論文 / 著書情報
Article / Book Information

題目(和文)	
Title(English)	Study on Chitosan Nanoparticle-Based Structures for Acoustic Cavitation Enhancement
著者(和文)	XIEXue
Author(English)	Xue Xie
出典(和文)	学位:博士(工学), 学位授与機関:東京科学大学, 報告番号:甲第353号, 授与年月日:2025年3月26日, 学位の種別:課程博士, 審査員:北本 仁孝,曽根 正人,和田 裕之,林 智広,中村 健太郎
Citation(English)	Degree:Doctor (Engineering), Conferring organization: Institute of Science Tokyo, Report number:甲第353号, Conferred date:2025/3/26, Degree Type:Course doctor, Examiner:,,,,
学位種別(和文)	博士論文
Type(English)	Doctoral Thesis

Study on Chitosan Nanoparticle-Based Structures for Acoustic Cavitation Enhancement

XIE Xue

Doctoral Dissertation

submitted to the

Department of Materials Science and Engineering

School of Materials and Chemical Technology

Institute of Science Tokyo

in partial fulfillment of the requirements for the degree of

Doctor of Engineering

Human Centered Science and Biomedical Engineering Major

February 2025

Doctoral supervisor: Professor Yoshitaka Kitamoto

Abstract

Ultrasound can be used in medical fields such as drug delivery and ultrasound imaging, as well as in chemical and industrial fields. The mechanism of the acoustic cavitation effect has been widely discussed and is considered to play an important role in these applications. The introduction of proper additives into the liquid medium under the ultrasound transducer can further enhance the cavitation effect. In this study, a composite structure with chitosan nanoparticles as the shell to stabilize the air cores has been proposed. The structure is designed to enhance ultrasonic cavitation mainly by introducing more cavitation nuclei utilizing the surface hydrophobicity of chitosan chains and providing acoustic microstreaming to accelerate rectified diffusion with the air cores. Chitosan nanoparticle-shelled composites were prepared by emulsifying a solution containing anionic surfactants (SDS) and cationic nanoparticles like chitosan nanoparticles. The characteristics of the composites can be controlled by manipulating the synthesis parameters. The drug loading ability of chitosan nanoparticles has been examined with a protein as the model drug. Furthermore, the composites' ability to enhance the acoustic cavitation effect was assessed by iodide dosimetry and terephthalic acid dosimetry during ultrasonic irradiation experiments with a frequency of 20 kHz. The composite has a recognized boosting influence on ultrasonic acoustic cavitation, as shown by KI dosimetry, and the trend of the calculated results agrees with the experimental data from TA dosimetry. This research has shown the promising possibilities of combining chitosan and microbubbles.

Table of Contents

List of Figures

List of Tables

Chapter 1 General Introduction

Ultrasound is extensively used in medical and chemical fields due to its safety, low cost, and ease of combination with other techniques. Over the past few decades, ultrasound has emerged as a critical tool in medicine, used for therapeutic and diagnostic purposes. Its non-invasive nature and the ability to deliver precise energy to targeted areas have made it an essential modality in modern healthcare. The therapeutic use of ultrasound, particularly in breaking kidney stones through lithotripsy, has revolutionized treatment options, offering a non-surgical alternative that is both effective and patient-friendly. Additionally, ultrasound's role in tumor treatment, thrombolytic therapy, and the delivery of medicine and genetic material underscores its versatility and importance in advancing medical treatments. Ultrasound imaging stands out as a widely respected clinical imaging method, providing real-time quantitative information on human anatomy and physiology. Its application spans various clinical fields, including obstetrics, cardiology, and oncology, primarily for the diagnosis of cancer and other disorders. The development of advanced imaging techniques, such as 3D imaging systems, contrast agents, and the integration of artificial intelligence, has further enhanced the diagnostic capabilities of ultrasound, making it an indispensable tool in clinical practice. Ultrasound's role in drug delivery is another area of significant interest. Techniques such as sonophoresis and sonoporation leverage ultrasound to enhance the permeability of the skin and cell membranes, respectively, facilitating the delivery of drugs into the body. This approach has shown promise in improving the efficacy of topical and systemic drug treatments, although more research is needed to fully understand and optimize these methods for clinical use [1–4].

In the chemical field, power ultrasound represents a promising tool for green and sustainable chemical processing. The phenomenon of acoustic cavitation, where rapidly collapsing bubbles in liquids create intense localized energy, accelerates chemical

reactions and improves catalyst effectiveness. Furthermore, ultrasound has emerged as an advanced oxidation process for water and wastewater treatment, offering a potent method for degrading organic pollutants and enhancing biodegradability [5–7].

A deeper understanding of the mechanisms underlying ultrasound, including thermal effects, acoustic cavitation, and other mechanical effects like acoustic streaming, is crucial for optimizing its use in various applications. Acoustic cavitation, in particular, is a key mechanism that facilitates chemical and physical changes in liquids, enhancing processes such as mixing, emulsification, and nanoparticle synthesis. Despite its numerous advantages, the use of ultrasound is not without challenges. Issues such as non-uniform heating, potential material damage, and the complexity of scaling up processes must be addressed to fully harness the benefits of this technology [2,4,7–9].

Ultrasonic applications may benefit from the creation and use of chitosan nanoparticles and microbubbles, which mark a noteworthy breakthrough in materials science. Chitosan, a biocompatible and biodegradable polymer, is used to create nanoparticles and microbubbles for drug delivery, gene therapy, and ultrasound imaging. These systems offer improved drug solubility, stability, and bioavailability while reducing toxicity. The synthesis methods, advantages, and challenges associated with chitosan-based systems are explored, highlighting their potential to enhance therapeutic efficacy and diagnostic accuracy [10–13].

In drug delivery, chitosan nanoparticles protect drugs from degradation and facilitate their delivery to target sites, including crossing biological barriers like the blood-brain barrier. For gene therapy, chitosan nanoparticles enhance the transfer of genetic material into cells, although transfection efficiency remains a challenge. Despite the advancements, challenges remain in the development of chitosan nanoparticles and chitosan-based microbubbles. Issues such as poor solubility of chitosan, limited drug

loading capacity, and enhancing ultrasonic performance with chitosan-based microbubbles need to be addressed. Future research aims to optimize synthesis methods, improve targeting and release properties, ensure biocompatibility and safety, and assess the effect on ultrasonic applications. The exploration of multifunctional chitosan-based structures that can simultaneously deliver multiple drugs or combine therapeutic and diagnostic functions represents an exciting area of research with significant potential for innovative solutions in medicine and biotechnology [10,14–16].

1.1 Applications of ultrasound in medical and chemical field

1.1.1 In medicine

Over the past decades, ultrasound has been applied in the medical field for therapeutic and diagnostic purposes. The benefits of ultrasound have been investigated by different research teams around the world. The treatment of ultrasound has rapidly replaced surgery for breaking kidney stones since the 1980s, using focused ultrasonic energy or shock waves directly and noninvasively to the stones [2]. Consequently, the development of therapeutic ultrasound has advanced rapidly with a great many strategies presently being used. Furthermore, recent studies point to exciting new clinical applications for ultrasound, including thrombolytic therapy, tumor treatment, and the delivery of medications and genetic material [8]. A deeper comprehension of the processes through which ultrasound interacts with tissues are necessary in both diagnostic and therapeutic uses of ultrasound.

Ultrasound Imaging

A well-respected clinical imaging method that offers quantitative, real-time information on human anatomy and physiology is ultrasound imaging. It is one of the most widely used clinical imaging techniques and is increasingly being utilized to guide

interventional clinical treatments considering its low cost of obtaining and maintaining and lack of ionizing radiation. Because laboratory mice and human lives differ in size and heart rate, translating clinical ultrasound practices to preclinical applications proved to be a substantial technological challenge until 20 years ago [3]. Ultrasound imaging is mostly used in the clinical fields of obstetrics and cardiology (heart, blood vessels, thyroid, and abdomen), primarily for the diagnosis of cancer and other disorders [17].

Conventional two-dimensional ultrasound imaging has been widely used because it can dynamically display 2D images of the region of interest in real-time [18]. An ultrasound transducer emits ultrasound waves. The transducer's frequency selection is crucial since higher frequencies improve spatial resolution but also limit the depth at which meaningful information can be extracted [19]. Since 2D ultrasound imaging can only provide a limited view of anatomy, it is challenging to visualize the complete 3D structure and understand the spatial relationships between organs and tissues. To solve this problem and improve diagnostic efficiency, 3D imaging systems [20], techniques like strain or shear wave imaging [21,22], contrast agents [23] and the use of artificial intelligence are interesting topics that are being evaluated.

Ultrasound contrast agents are microbubbles that can be injected into a patient's bloodstream to improve the quality of ultrasound images. These microbubbles can stay in the circulation for many minutes due to the poor solubility of the gas core and shell; in contrast, unencapsulated air bubbles of the same size would disintegrate in milliseconds. The diameter of commercial ultrasonic contrast agent microbubbles ranges from 1 to 5 microns [24], which is about equivalent to the size range of blood cells. As a result, they are sufficiently tiny to enter the pulmonary circulation unharmed [1,25].

Therapeutic Ultrasound

Tissue heating results from the absorption of ultrasonic energy, and this has been applied therapeutically in a variety of situations. It has been discovered more recently that there may be advantages to the non-thermal actions that happen when ultrasound passes into tissue. Ultrasound treatments may be roughly classified into two categories: "low" power therapies, which include sonophoresis, gene therapy, and bone healing, and "high" power therapies, which include lithotripsy and high-intensity focused ultrasound [26].

Physical therapy involved with ultrasound is mostly used to treat soft tissue injuries, speed up the healing process, reduce edema, and soften scar tissue. Among other things, cardiovascular issues and bone injuries are also treated with it. It's still unclear how much the patient may gain clinically from physical therapy ultrasound treatments [27]. However, when the modality is used correctly, the danger of injury, such as burns, seems to be minimal. Hyperthermia was the focus of much work in the 1980s and 1990s, which was the method of ultrasonically heating relatively large amounts of tissue for the purpose of cancer treatment. This hyperthermia technique seems to work by evenly heating a tumor to around 42°C at intervals of approximately one hour [28]. The focus of hyperthermia cancer treatment has changed to high intensity focused ultrasound, as the moderate-temperature hyperthermia approach has not gained traction in clinical treatments [2]. High intensity focused ultrasound uses highly focused ultrasound beams to create small, intense heat zones at a targeted location. It is approved for various applications including treating uterine fibroids [29], prostate cancer [30], and aesthetic procedures. However, it can also cause side effects like burns, pain, and bleeding [31]. Lithotripsy is a well-established, non-invasive treatment for kidney stones. Over the past three decades, lithotripsy technology has improved significantly, but its success rate depends on various factors. To optimize results and minimize the need for repeat procedures, doctors carefully select patients for lithotripsy based on body size, stone

characteristics, and location. Researchers are actively exploring methods to improve lithotripsy outcomes. One area of focus is cavitation, the creation and collapse of bubbles in fluids, which is crucial for stone fragmentation. New techniques are being developed to enhance cavitation and its effectiveness in breaking down stones [32]. Ultrasound therapy shows promise as a way to accelerate bone healing, but more research is needed to solidify its effectiveness. Low-intensity ultrasound appears to be beneficial, while high-intensity ultrasound can actually hinder healing. The exact mechanism by which low-intensity ultrasound promotes healing remains unclear, but it likely doesn't involve heat. More clinical studies are urgently required, especially for acute fractures that might turn into non-unions and for non-unions that are already established and need to be compared to the existing standard of treatment. The success of this treatment depends on a delicate balance of factors including the frequency, intensity, and timing of ultrasound application [33,34].

Drug Delivery

Ultrasound has the potential to improve the delivery of drugs into the body through the skin (sonophoresis) and into cells (sonoporation). Sonophoresis uses ultrasound to temporarily increase the permeability of the skin, allowing greater penetration of topically applied drugs. The exact mechanism is unclear, but it likely involves cavitation or streaming created by the ultrasound waves. Low frequencies (less than 100 kHz) appear to be more effective than high frequencies. While some studies have shown promise for pain relief and inflammatory responses, more research with better scientific rigor is needed [35–37]. Sonoporation uses ultrasound to transiently alter the structure of cell membranes, allowing for the uptake of drugs. Many studies have explored using ultrasound with various drugs, but most have been done in vitro and may not translate to real-world situations [38–40]. There is growing evidence that cavitation, either induced by ultrasound or facilitated by microbubbles introduced into the tissue, plays a key role in enhancing drug delivery. Microbubbles can be used to

carry drugs, or they can be used to increase the permeability of blood vessels or the blood-brain barrier to allow for the passive transport of drugs [41].

Ultrasound is also being explored for its potential to facilitate gene therapy by enhancing the transfer of genes into diseased tissues. Ultrasound can improve gene transfer, especially in the presence of cavitation. There are two main types of gene transfer vectors being studied: viral and non-viral. Non-viral vectors are easier to prepare and microbubbles can be used to deliver genes [42–44]. Overall, ultrasound is a promising tool for enhancing drug and gene delivery. Research in this area is ongoing, and future applications may include non-invasive treatments for a variety of conditions.

1.1.2 In chemical

Power ultrasound is a promising tool for green and sustainable chemical processing. Its effectiveness relies on a phenomenon called acoustic cavitation, where rapidly collapsing bubbles in liquids create intense localized energy [6]. This energy can significantly speed up chemical reactions, leading to higher product yields in shorter times. Research has shown that power ultrasound can benefit various chemical reactions, including Mannich-type reactions [45], Aza-Michael reactions [46], and catalytic processes [47]. The benefits include faster reaction rates, reduced energy consumption, improved catalyst effectiveness and safer processes. Sonochemical reactors have been built and investigated in terms of controlling mechanisms, reaction kinetics, and ideal operation parameters in order to advance the use of power ultrasound in chemical processes. For the sonochemical reactors, there are essentially two kinds of ultrasonic irradiation modes: direct, where the ultrasonic transducer is in direct contact with the reaction medium, and indirect, where it is mounted to the vessel's wall or bottom and not in direct contact with the reactants [48]. Higher power generally leads to faster reactions, but there is an optimal limit beyond which further increases have minimal impact. Higher frequencies enhance chemical effects but decrease physical

effects like mixing, so finding the optimal frequency is crucial.

In addition, ultrasound has emerged as a promising advanced oxidation process for water and wastewater decontamination in recent decades. Its effectiveness stems from its ability to generate extreme reaction conditions during sonication, leading to the thermal decomposition of water and the production of hydroxyl radicals. These powerful radicals degrade various organic pollutants, including emerging micropollutants, through direct pyrolysis and radical reactions [49,50]. Research suggests that ultrasound can be employed at different stages of water treatment. It can be used as a pre-treatment method to enhance biodegradability and reduce toxicity before secondary biological treatment [51,52]. Additionally, it functions as an effective post-treatment option for eliminating refractory compounds that persist after primary treatment [53]. While most studies have been conducted on a laboratory scale, the potential benefits of ultrasound are undeniable. Compared to alternative methods like ozonation or UV photolysis, ultrasound offers several advantages. It requires minimal maintenance and boasts greater energy efficiency. Notably, ultrasound waves, unlike UV light, can penetrate even opaque water systems. This makes it particularly attractive for treating wastewater with high turbidity or suspended solids, where the efficiency of other processes might decline [54]. The reaction mechanism can be tailored by adjusting various parameters. For instance, the addition of solid particles or gases can enhance cavitational intensity and efficiency if pyrolysis is the dominant mechanism.

Beyond pollutant degradation, ultrasound irradiation also holds promise for disinfection. However, achieving complete kill rates often requires high intensities, potentially increasing the cost. Nevertheless, combining ultrasound with existing disinfection techniques like chlorination, ozonation, or ultraviolet light has shown promise in enhancing effectiveness against microorganisms resistant to conventional methods. Studies suggest that low-frequency ultrasound coupled with various disinfectants,

adsorbents, or photocatalysts can achieve excellent results [55,56]. The efficiency of these combined treatments depends on factors like ultrasound intensity and frequency, irradiation time, and specific water characteristics. While research on viral removal with ultrasound is limited, the overall potential for decontamination across various stages of water treatment is significant.

Besides, one possible approach to raising the effectiveness of enhanced oil recovery is the use of ultrasonic oil production techniques. It has a number of benefits, including great versatility, ease of use, affordability, and little influence on the environment [57]. By inhibiting paraffin precipitation, lowering the viscosity of crude oil, encouraging demulsification and dehydration, eliminating clogging, and avoiding or lessening scaling, ultrasound enhances oil output [58]. Ongoing research endeavors aimed at refining ultrasonic irradiation parameters and creating sophisticated transducers have considerable potential for attaining increased efficacy and wider relevance within the field of enhanced oil recovery [59,60]. These are only a few of the ways ultrasound can be employed in the chemical industry. Further investigation into ultrasound has great promise for improving efficiency and expanding its use by modifying the ultrasonic irradiation parameters.

1.2 Ultrasound mechanisms and issues

There is potential for biological impacts to be produced by ultrasonic energy. In diagnostic applications, bioeffects can be prevented or planned for therapeutic reasons if exposimetry and etiology are well understood. In addition to heating, ultrasound treatment can also be used to produce effects by nonthermal mechanisms such as mechanical stress, gas body activation, ultrasonic cavitation, and other as-yet-unidentified nonthermal processes. The ultrasonic wave may deform when the pressure amplitude, frequency, or propagation length increases; this might finally result in a

discontinuity or shock in the waveform. In terms of bioeffects, increasing the pulse length, frequency, or nonlinear acoustic distortion might strengthen some nonthermal processes, such as radiation force, and raise heating.

There is a tendency for all bioeffect pathways to grow in likelihood and size as power or intensity is increased. Certain devices tend to create shocked or distorted waves due to their operation at greater amplitudes. The heat caused by ultrasound is the outcome of biological tissue absorbing acoustic radiation [61]. When it comes to diagnostic ultrasound, temperature rises and the possibility of bioeffects are maintained to a minimum or eliminated by using the as low as practically possible principle, limiting temporal average intensities, and often brief exposure times. The amplitude of the rarefactional pressure of ultrasonic waves is crucial for the processes of ultrasonic cavitation and gas body activation, which are intimately linked. It is possible for ultrasound waves to enter tissues with rarefactional pressure amplitudes of several megapascals. When appropriate cavitation nuclei are available, this high rarefactional pressure might operate to start cavitation activity in tissue. Alternatively, it can directly cause the pulsation of preexisting gas bodies, such as those found in the lung and gut, or with ultrasonic contrast agents [62–64]. The chance of cavitation and gas body activation rises with decreasing frequency. Additional potential mechanisms for the biological effects caused by ultrasound include the direct operation of shear, tensile, and compression stresses. In addition, radiation pressure, forces on particles, and acoustic streaming are examples of second-order phenomena that rely on transmitted ultrasonic energy [4].

Acoustic Cavitation

Acoustic cavitation is one of the most impactful mechanisms of ultrasound, characterized by the formation, growth, and implosive collapse of bubbles in a liquid medium. This process releases highly localized energy in the form of intense heat and

pressure, which can induce chemical and physical changes within the medium [5]. The implosion of cavitation bubbles generates microjets and shockwaves, which contribute to the mixing and homogenization of substances in the liquid. The high temperatures and pressures associated with cavitation bubbles can generate reactive species such as hydroxyl radicals and hydrogen peroxide. These reactive species are essential in sonochemical reactions, where they facilitate various chemical transformations, including oxidation and degradation processes. For example, in wastewater treatment, acoustic cavitation is utilized to break down complex organic pollutants into simpler, less harmful compounds, enhancing the overall efficiency of the treatment process [65,66].

In the context of material science, acoustic cavitation is employed in the synthesis of nanoparticles. The extreme conditions within collapsing cavitation bubbles provide a unique environment for the nucleation and growth of nanoparticles, allowing for the production of particles with controlled size and morphology. This method is advantageous over conventional synthesis techniques, as it often requires milder conditions and shorter reaction times [67]. Acoustic cavitation also finds applications in ultrasonic cleaning, where the implosion of bubbles effectively removes contaminants from surfaces [68]. This technique is widely used in industries requiring precision cleaning, such as electronics and medical device manufacturing. In the biomedical field, acoustic cavitation plays a pivotal role in therapeutic ultrasound applications, such as lithotripsy and sonoporation. These applications underscore the versatility and efficacy of cavitation in medical treatments.

Despite the numerous advantages and diverse applications of acoustic cavitation, there are notable limitations that can affect its effectiveness. One major limitation is the difficulty of controlling the cavitation process. The formation, growth, and collapse of cavitation bubbles are highly dependent on the acoustic frequency, intensity, and

properties of the liquid medium, making it challenging to achieve consistent and reproducible results [69]. Additionally, the intense localized energy released during bubble collapse can cause damage to materials and surfaces, limiting its use in processes involving delicate or sensitive components. The harsh conditions generated by cavitation can also lead to the degradation of certain chemicals or materials, reducing their effectiveness or lifespan. Furthermore, the scale-up of cavitation processes from laboratory to industrial scale can be complex and cost-intensive, often requiring specialized equipment and careful optimization to ensure efficiency and safety [7,70]. These limitations necessitate careful consideration and optimization when applying acoustic cavitation in practical scenarios, balancing its benefits with potential drawbacks to achieve the desired outcomes.

Thermal Effects

Ultrasound's thermal effects play a crucial role in various industrial applications, significantly impacting heat transfer processes. When ultrasonic waves propagate through a medium, they generate localized heating due to the absorption of acoustic energy. This phenomenon can be leveraged to enhance convective heat transfer in liquids, where the thermal boundary layer is reduced, promoting more efficient heat exchange [61]. Studies have demonstrated that the application of power ultrasound can increase the Nusselt number—a dimensionless measure of heat transfer efficiency—substantially, depending on the ultrasonic intensity and positioning relative to the heat source [71]. The ultrasonic waves can also disrupt fouling layers on heat exchanger surfaces, which is a major challenge in maintaining efficient heat transfer in industrial systems. By preventing the accumulation of fouling, ultrasonic treatment ensures the sustained high performance of heat exchangers [72,73]. For instance, experimental results indicate that lower acoustic frequencies achieve better antifouling effects compared to higher frequencies. Additionally, the cavitation bubbles generated by ultrasonic waves promote the nucleation and release of boiling bubbles, further

enhancing heat transfer in subcooled boiling conditions [74,75].

In the realm of food processing, ultrasonic heating has emerged as a non-invasive method to pasteurize and sterilize liquid foods. The localized heat generated by ultrasonic waves can inactivate microorganisms without significantly affecting the nutritional and sensory qualities of the food product [76–78]. This method offers a significant advantage over traditional thermal treatments, which often degrade the quality of food due to excessive heat exposure. The enhancement of heat transfer through ultrasonic waves has potential applications in various fields, including chemical processing, where maintaining optimal temperatures is crucial for reaction efficiency. For instance, in catalytic reactions, ultrasound can uniformly distribute heat, ensuring consistent reaction rates across the catalyst bed. This can lead to higher yields and more efficient use of reactants [79]. The ability to control and manipulate heat transfer processes with ultrasound offers a valuable tool for industries seeking to improve energy efficiency and process reliability.

Ultrasound's thermal effects are subject to a number of restrictions that may limit its use in certain contexts. One significant limitation is the potential for non-uniform heating, which can lead to localized hotspots within the medium. This uneven distribution of heat can cause thermal gradients, resulting in inconsistent processing outcomes or damage to heat-sensitive materials [80]. Another challenge is the potential for excessive heating, which can degrade the quality of certain products, particularly in food processing where maintaining nutritional and sensory attributes is crucial [81]. Additionally, the efficiency of ultrasonic heating is highly dependent on the acoustic properties of the medium, including its viscosity, density, and thermal conductivity. These factors can influence the absorption and distribution of acoustic energy, making it difficult to achieve uniform and controlled heating in complex or heterogeneous systems [82]. Moreover, the generation of heat through ultrasound can lead to a rapid

increase in temperature, which may necessitate additional cooling mechanisms to prevent overheating and ensure process stability. This can increase the complexity and cost of the equipment required for ultrasonic heating applications. Lastly, while ultrasound can enhance heat transfer, it may not always be sufficient to replace conventional heating methods entirely, particularly in large-scale industrial processes where the heat input from ultrasound alone might be inadequate to meet the required thermal load [6,71]. These limitations highlight the need for careful optimization and integration of ultrasound with other thermal management strategies to achieve effective and efficient heating outcomes.

Other Mechanical Effects

Beyond thermal effects and cavitation, ultrasound induces various other mechanical effects. One such effect is acoustic streaming, which refers to the steady flow of the liquid medium caused by the absorption of acoustic energy [75]. Acoustic streaming enhances mass transfer rates, which is particularly useful in processes such as mixing, emulsification, and extraction. For instance, ultrasound-assisted extraction leverages acoustic streaming to improve the efficiency of extracting valuable compounds from plant materials, significantly reducing processing times and solvent usage [83]. In the realm of pharmaceuticals, acoustic streaming is utilized to enhance the dissolution rates of poorly soluble drugs. By creating micro-mixing zones, ultrasound ensures a more uniform distribution of the drug particles in the solvent, leading to faster and more complete dissolution. This is particularly important in the formulation of oral medications, where rapid and consistent drug release is critical for therapeutic efficacy [84,85].

Ultrasonic waves can also cause the disintegration of cellular structures, making them highly effective in processes like cell disruption and homogenization. This mechanical effect is widely used in the biotechnology and pharmaceutical industries for the

extraction of intracellular contents and the preparation of emulsions and suspensions. The ability to control the intensity and duration of ultrasonic exposure allows for precise manipulation of the process parameters, ensuring optimal results without compromising the integrity of sensitive biological materials. In aerosol applications, high-intensity acoustic fields cause particle agglomeration via hydrodynamic and orthokinetic interactions, among other causes. In industrial gas cleaning, this procedure is implemented to enable small particles to clump together into bigger aggregates that are easily removed using standard filtering techniques. The practical use of acoustic aggregation in dust removal demonstrates the adaptability of ultrasound to tackle health and environmental issues related to airborne particulate matter [86]. Ultrasound also enhances the degassing of liquids by facilitating the coalescence and release of dissolved gases. This is particularly useful in industries such as metallurgy, where the presence of dissolved gases in molten metals can lead to defects in the final product [87,88]. By using ultrasound, manufacturers can produce higher-quality metal castings with fewer imperfections. The rapid and efficient removal of gases also improves the overall process efficiency and product quality.

In summary, the various mechanical effects of ultrasound offer significant advantages across a wide range of medical and industrial fields. These effects enhance process efficiency, reduce operational costs, and contribute to the development of sustainable and environmentally friendly technologies. Despite its numerous advantages, the use of ultrasound in various applications is limited by several factors [6,89]. High equipment costs and maintenance requirements, increased energy consumption, and the complexity of scaling up from laboratory to industrial processes are significant challenges. Acoustic shadowing and reflection in heterogeneous media can lead to uneven treatment, while safety concerns, such as hearing damage and potential biological effects, necessitate stringent safety measures. Additionally, chemical compatibility issues, regulatory and environmental constraints, and the need for precise

control of thermal effects in temperature-sensitive applications further complicate the use of ultrasound. These limitations require careful optimization and thorough understanding to effectively harness the benefits of ultrasound technology.

1.3 Chitosan nanocarriers

Chitosan nanoparticles have garnered significant attention in recent years due to their exceptional properties, including biocompatibility, biodegradability, and ease of modification. Chitosan, a copolymer containing β-(1,4)-2-acetamido-D-glucose and β-(1,4)-2-amino-D-glucose units, is derived from chitin through deacetylation [90]. The molecular weight and degree of deacetylation of chitosan greatly influence its properties, making it a versatile material for various applications. Chitosan's unique ability to form gels, films, and nanoparticles upon protonation under acidic conditions further enhances its applicability in biomedical fields [91].

The synthesis of chitosan nanoparticles (CNP) can be achieved through several methods, each with its advantages and limitations. Ionic cross-linking is a widely used method where chitosan interacts with a cross-linking agent, such as sodium tripolyphosphate, to form nanoparticles [92]. This method avoids organic solvents and operates at room temperature, producing uniform nanoparticles suitable for protein and gene drug encapsulation. However, controlling particle size and achieving high drug loading can be challenging. Covalent cross-linking involves forming covalent bonds between chitosan and functional cross-linking agents like glutaraldehyde, producing stable nanoparticles with specific properties but potentially introducing toxicity due to residual cross-linking agents [93]. Precipitation methods, including desolvation and diffusion of emulsified solvents, offer simple synthesis routes but often result in large particles with limited applications. For instance, the desolvation method decreases chitosan solubility using flocculants, leading to nanoparticle formation [94]. In contrast,

the emulsified solvent diffusion method uses turbulence between water and organic phases to precipitate chitosan, resulting in the generation of nanoparticles [95]. Although these techniques are simple, the final particles generated may be huge, and their use may be limited.

Polymerization techniques, such as radical polymerization, allow for precise control over nanoparticle properties by combining different monomers [96]. Radical polymerization methods enable the creation of core-shell nanoparticles with tailored properties, although the process can be complex and require stringent conditions. For example, chitosan-poly(isobutyl cyanoacrylate) nanoparticles prepared via this method exhibit a uniform spherical shape and consistent size distribution [97]. Self-assembly of amphiphilic compounds forms nanoparticles with core-shell structures, providing a hydrophobic core for drug encapsulation and a hydrophilic shell for stability in biological environments [98,99]. This method excels at delivering both hydrophobic and hydrophilic drugs but may suffer from low drug loading efficiency. Modified amphiphilic chitosan derivatives, such as those using cholanic acid or glycol chitosan, have shown promise in enhancing drug solubility and stability [100]. Spray-drying is another method used to prepare chitosan nanoparticles. This technique involves spraying a solution containing chitosan and the drug into a hot chamber, causing rapid evaporation of the solvent and the formation of nanoparticles. Spray-drying can produce nanoparticles in a single step and is scalable for industrial applications. However, controlling the size and distribution of nanoparticles can be challenging [101,102].

The applications of chitosan nanoparticles are extensive, spanning drug delivery, gene therapy, antibacterial treatments, and beyond. As drug carriers, they enhance drug solubility, stability, and bioavailability while reducing toxicity. Chitosan nanoparticles can cross biological barriers, such as the blood-brain barrier, delivering drugs to target

sites effectively [103]. For instance, they have been employed in delivering anticancer drugs like doxorubicin [104] and paclitaxel [105], enhancing therapeutic efficacy and reducing side effects. In gene therapy, chitosan nanoparticles protect genetic material from degradation and facilitate cellular uptake, although transfection efficiency remains a challenge [106]. The positive surface charge of chitosan facilitates its interaction with negatively charged genetic materials, forming stable complexes that can be internalized by cells. For protein drugs, chitosan nanoparticles improve bioavailability and protect against enzymatic degradation, though controlling release kinetics can be difficult [107,108]. Studies have shown that encapsulating proteins like insulin in chitosan nanoparticles can protect them from degradation in the gastrointestinal tract and enhance their absorption [109]. Recent research has focused on modifying chitosan nanoparticles to enhance their functionality. pH-sensitive chitosan nanoparticles release drugs in response to environmental pH changes, making them suitable for targeting acidic tumor microenvironments. For example, chitosan nanoparticles modified with poly(propyl acrylic acid) exhibit increased drug release in acidic conditions, enhancing their potential for cancer therapy [110,111]. Thermosensitive chitosan nanoparticles release drugs at specific temperatures, potentially improving the efficacy of hyperthermia treatments. Chitosan-poly(N-isopropylacrylamide) graft copolymer nanoparticles, for example, release drugs at temperatures above 38°C, targeting hyperthermic tumor cells while sparing normal tissues [112,113]. Targeting modifications, such as ligand attachment, improve the specificity of drug delivery to particular tissues or cells, enhancing therapeutic outcomes and reducing side effects. Ligands like folic acid can be attached to chitosan nanoparticles to enhance their targeting ability against cancer cells [114]. In antibacterial applications, chitosan nanoparticles exhibit strong antibacterial activity due to their positive charge, which interacts with the negatively charged bacterial cell membranes, causing disruption and cell death. Chitosan nanoparticles loaded with various metal ions, such as silver or copper, have shown enhanced antibacterial properties. These nanoparticles can be used

in wound dressings, coatings for medical devices, and as preservatives in food packaging [115].

Despite the advancements, challenges remain in the development of chitosan nanoparticles. Issues such as poor solubility of chitosan, limited drug loading capacity, and potential toxicity of modified chitosan derivatives need to be addressed [116,117]. Chitosan's poor solubility in neutral and basic conditions limits its application, necessitating chemical modifications to improve its solubility and functionality. Moreover, while chitosan nanoparticles can encapsulate hydrophilic drugs effectively, encapsulating hydrophobic drugs often requires additional modifications or surfactants, which can affect biocompatibility. Future research aims to overcome these limitations, focusing on optimizing synthesis methods, improving targeting and release properties, and ensuring biocompatibility and safety. Developing multifunctional chitosan nanoparticles that can simultaneously deliver multiple drugs or combine therapeutic and diagnostic functions is an exciting area of research. Additionally, exploring the use of chitosan nanoparticles in emerging fields such as immunotherapy, regenerative medicine, and environmental applications holds great promise. The future of chitosan nanoparticles lies in their ability to adapt to diverse applications, offering innovative solutions in medicine, biotechnology, and beyond.

1.4 Microbubbles & Chitosan nanoparticle-shelled composites

Microbubbles, defined as gas-filled bubbles with diameters in the micron range, have garnered significant attention due to their unique properties and extensive applications in biomedical fields [118]. Comprising a gas core surrounded by a stabilizing shell made of lipids, proteins, polymers, or surfactants, microbubbles enhance ultrasound contrast and act as a vehicle for drug delivery [16]. Their synthesis can be achieved through various methods, each with specific advantages and limitations. Sonication

involves using ultrasound waves to create microbubbles from a liquid medium. This technique is simple and efficient but may result in a wide size distribution [119,120]. Mechanical agitation uses mechanical forces such as shaking or stirring to produce microbubbles, commonly applied for large-scale production but potentially yielding heterogeneous size distributions [121,122]. Electrolysis, wherein an electric current generates gas bubbles in a liquid, is another method but is less commonly used in biomedical applications due to difficulty in controlling bubble size [123]. Additionally, microfluidic techniques allow precise control over bubble size and uniformity, albeit with limitations in scalability [124,125].

Microbubbles can be classified based on their shell materials, including lipid, protein, and polymeric microbubbles. Lipid microbubbles, formed from phospholipids, are biocompatible and offer flexible and thin shells, but they are prone to gas diffusion and collapse [126]. Protein microbubbles, typically using albumin, provide stability but may have immunogenicity concerns [127,128]. Polymeric microbubbles, using materials such as poly(lactic-co-glycolic acid) (PLGA), offer greater stability and tunable properties but normally involve more complex synthesis processes [129,130].

Ultrasound-involved applications of microbubbles are primarily in diagnostic imaging and therapeutic delivery. In ultrasound imaging, microbubbles serve as contrast agents, significantly enhancing the quality of the images by reflecting sound waves. They improve the visualization of blood flow and tissue perfusion, aiding in the diagnosis of various cardiovascular and oncological conditions [131,132]. In therapeutic applications, microbubbles can be used for drug delivery, where their shells encapsulate therapeutic agents. Upon ultrasound exposure, the microbubbles can be targeted to specific tissues, and the ultrasound waves can induce cavitation, releasing the drug precisely at the target site. This targeted delivery enhances drug efficacy and reduces systemic side effects [133,134]. Microbubbles are also used in gene therapy, where they

facilitate the delivery of genetic material into cells [135,136]. The positive charge of certain microbubble shells interacts with the negatively charged cell membranes and genetic material, promoting cellular uptake and protecting the genetic payload from degradation. Additionally, microbubbles are investigated for their potential to enhance the delivery of oxygen and other gases in medical treatments, providing targeted and efficient transport to tissues in need [137,138].

However, microbubbles have certain limitations. Their stability is a major concern, as they can collapse or coalesce under pressure or over time, limiting their shelf life and in vivo performance. Size control during synthesis can also be challenging, affecting their uniformity and, consequently, their behavior in biological systems. Additionally, while they enhance ultrasound imaging, the resolution is still inferior to other imaging modalities like MRI or CT, and the depth of penetration is limited. Moreover, the potential immunogenicity and toxicity of the materials used for the shell must be carefully evaluated to ensure safety in clinical applications [14,139].

Chitosan microbubbles have emerged as a promising tool in the fields of targeted drug delivery and gene therapy due to their unique properties and multifunctional capabilities. The merits of chitosan microbubbles include their biocompatibility, biodegradability, and ability to provide targeted delivery with minimal side effects. Chitosan microbubbles are synthesized using various techniques, with each method tailored to achieve specific characteristics required for different applications. The common synthesis method involves the formation of a core-shell structure, where the core is typically composed of a gas or volatile liquid, such as perfluoropentane, and the shell is made of chitosan [140,141]. Then the emulsification-solvent evaporation technique is frequently employed, wherein an organic solvent containing the core material is emulsified in an aqueous chitosan solution. Upon solvent evaporation, chitosan forms a stable shell around the core. Another method involves the use of high-intensity

ultrasound to produce nanodroplets that transition into microbubbles upon exposure to ultrasound, a process known as acoustic droplet vaporization [142].

The applications of chitosan microbubbles are vast and diverse, primarily focusing on their use as carriers for drug delivery and gene therapy. They can encapsulate therapeutic agents, including chemotherapeutic drugs, genes, and proteins, and release them in a controlled manner at the target site [105,121]. This targeted delivery is facilitated by the application of ultrasound, which triggers the release of the encapsulated agents through cavitation or sonoporation. Chitosan microbubbles have shown potential in enhancing the efficacy of cancer treatments, improving the transfection efficiency in gene therapy, and providing non-invasive imaging contrast in molecular imaging [143–146]. Chitosan's positive charge allows for easy complexation with negatively charged nucleotides, enhancing the stability and protection of the genetic material during delivery. Additionally, the use of ultrasound as a trigger for drug release offers precise spatial and temporal control, reducing systemic toxicity and improving therapeutic outcomes. Several studies have focused on enhancing the functionality of chitosan microbubbles through various modifications. pH-sensitive chitosan microbubbles release their payload in response to environmental pH changes, making them suitable for targeting acidic tumor microenvironments [147]. Thermosensitive chitosan microbubbles release drugs at specific temperatures, potentially improving the efficacy of hyperthermia treatments [148]. Targeting modifications, such as ligand attachment, improve the specificity of drug delivery to particular tissues or cells, enhancing therapeutic outcomes and reducing side effects. Chitosan microbubbles are also being explored for their potential in regenerative medicine. Their ability to encapsulate and deliver growth factors and other bioactive molecules makes them suitable for promoting tissue repair and regeneration. For instance, chitosan microbubbles loaded with vascular endothelial growth factor (VEGF) have been studied for enhancing angiogenesis in ischemic tissues [149,150].

Additionally, chitosan's natural antimicrobial properties can be leveraged in wound healing applications, where chitosan microbubbles can deliver antimicrobial agents to infection sites, promoting healing while preventing bacterial growth [151].

However, there are limitations associated with chitosan microbubbles. The synthesis process can be complex and may require optimization to achieve consistent and reproducible results. The stability of the microbubbles can be compromised under physiological conditions, and the potential for immune response activation by chitosan necessitates careful evaluation of dosage and administration routes. Furthermore, the efficiency of drug or gene delivery can be affected by factors such as bubble size, shell thickness, and ultrasound parameters, requiring extensive in vitro and in vivo studies to optimize these variables. Issues such as poor solubility of chitosan in neutral and basic conditions, limited drug loading capacity, and potential toxicity of modified chitosan derivatives need to be addressed [10–12,15,103]. Recent research has focused on overcoming these limitations and enhancing the functionality of chitosan microbubbles. Advances include the development of multifunctional microbubbles that combine drug delivery with diagnostic imaging, offering a theranostic approach. Surface modifications with targeting ligands have been explored to improve specificity towards diseased tissues. Studies have also investigated the use of chitosan derivatives and co-polymers to enhance the stability and reduce the immunogenicity of the microbubbles [10,152].

1.5 Purpose and significance of this study

Acoustic cavitation is a powerful phenomenon with numerous therapeutic and industrial applications. This process generates extreme conditions, such as high temperatures and pressures, which can be harnessed to enhance various physical and chemical processes. Acoustic cavitation occurs when ultrasonic waves create

alternating high-pressure and low-pressure cycles in a liquid. During the low-pressure phase, microscopic bubbles form and grow. In the subsequent high-pressure phase, these bubbles collapse violently, releasing significant energy in the form of shock waves and microjets. This energy release can induce localized heating, high shear forces, and rapid mixing, which are beneficial in numerous applications, such as heat transfer, chemical reactions, sonophoresis and sonoporation [4,5].

Enhancing the effect of acoustic cavitation can be achieved through various strategies, including optimizing the frequency and power of ultrasound, using appropriate liquid media, and incorporating additives [7]. The frequency and power of ultrasound are critical parameters that influence the intensity and distribution of cavitation bubbles. Studies have shown that lower frequencies (15 - 60 kHz) are generally more effective in generating larger cavitation bubbles, which collapse with greater intensity, thereby enhancing the cavitation effect. Increasing the ultrasonic power also intensifies the cavitation effect, although it may lead to acoustic streaming, which could alter the desired outcomes. An optimal balance between power and frequency is necessary to maximize the cavitation effect while minimizing unwanted side effects. The properties of the liquid medium, such as viscosity, surface tension, and vapor pressure, significantly impact cavitation dynamics. Liquids with lower viscosity and surface tension generally facilitate easier bubble formation and collapse. Additionally, the presence of dissolved gases can enhance cavitation by providing nucleation sites for bubble formation. Selecting or modifying the liquid medium to suit the specific application can significantly enhance cavitation effects.

The introduction of nanoparticles or other additives into the liquid medium can further enhance the cavitation effect. Nanoparticles provide additional nucleation sites for bubble formation, leading to increased cavitation activity. Studies have demonstrated that the use of nanoparticles can stabilize cavitation bubbles and enhance heat transfer

rates [12,153]. Some researchers reported that corrugated hydrophilic particles with diameters between 30 and 150 μm were observed to cause cavitation inception at their surfaces when they were exposed to a short, intensive tensile stress wave [154]. So these results leave 2 directions in drug carrier design: the first is to trap inherent gas bubbles in the carriers, and the second is to make the surface of the carriers not smooth. A dynamic equilibrium model studied the stability of nanobubbles partly covered with hydrophobic or hydrophilic materials in water. The result showed that a stable nanobubble could be present when the fraction of surface coverage by hydrophobic material was from about 0.5 to 1 while a nanobubble could only be stable when the fraction of surface coverage by hydrophilic material was exactly 1 [155].

Therefore in this study a complex structure with chitosan nanoparticles as the shell to stabilize the air cores has been proposed (Fig. 1). The structure is thought to enhance ultrasonic cavitation mainly by the following two mechanisms: 1, introducing more cavitation nuclei through the surface hydrophobicity of chitosan; and 2, the periodic growth and shrinking of nano-sized gas cores providing acoustic microstreaming to accelerate rectified diffusion. The repeating units of chitosan are β-(1→4)-linked glucosamines that constitute a large number of hydroxy and amino groups. These amino groups are suggested to be highly reactive, which can be utilized by chemical reactions in surface modification and protein attachment. Some researchers reported that modifying the surface hydrophobicity of chitosan by introducing positive and negative charges via methylation using methyl iodide (MeI) and reductive alkylation using 5-formyl-2-furan sulfonic acid (FFSA) can be tuned by adjusting the reaction time [156]. Chitosan-shelled nanobubbles were prepared by emulsifying a solution containing anionic surfactants (like SDS) and cationic nanoparticles like chitosan nanoparticles [121]. The size of nanobubbles can be controlled by manipulating the concentrations of nanoparticles or via other synthesis conditions such as stirring speed and time. For nano-sized gas cores, the frequency threshold for bubbles to undergo stable cavitation

would be higher than 1 MHz, which is around the limitation of therapeutic ultrasound [5]. For the ultrasound homogenizer whose frequency is 20 kHz, rectified diffusion will not occur so the small bubbles will not grow but due to the shell I assume they would not disappear. Then the gas cores undergo low amplitude sinusoidal radial pulsations, which are often referred to as a breathing mode and may induce acoustic microstreaming on the outer surface. Acoustic microstreaming, or cavitation microstreaming, refers to the small-scale streaming flow of fluid around an oscillating object such as a gas bubble and can serve to enhance mixing effects around a bubble. Therefore, the breathing mode of the core may increase the rate of bubble growth of the outer cavitation nuclei since microstreaming drives fresh solution with a higher gas concentration for rectified diffusion [5,157].

The goal of the study is to design a composite that effectively enhances acoustic cavitation, which is promising for drug delivery and the initiation of sonochemical reactions. Nanobubbles with chitosan as the shell have not been widely studied, which perhaps is due to the application of chitosan focusing on drug carriers. Chitosan is chosen for its biocompatibility, the ability to act as carriers and its changeable hydrophobicity, which are not possessed by metal materials or other polymers. This research demonstrate a simple process to prepare chitosan nanoparticle-shelled microbubbles, then prove their ability to load drugs and utilize iodide dosimetry and terephthalic acid dosimetry to assess the enhancement of the acoustic cavitation effect [158,159]. Developing multifunctional chitosan microbubbles that can simultaneously deliver multiple drugs or combine therapeutic and diagnostic functions is an exciting area of research. Additionally, exploring their use in emerging fields such as sonochemistry, regenerative medicine, and environmental applications holds great promise.

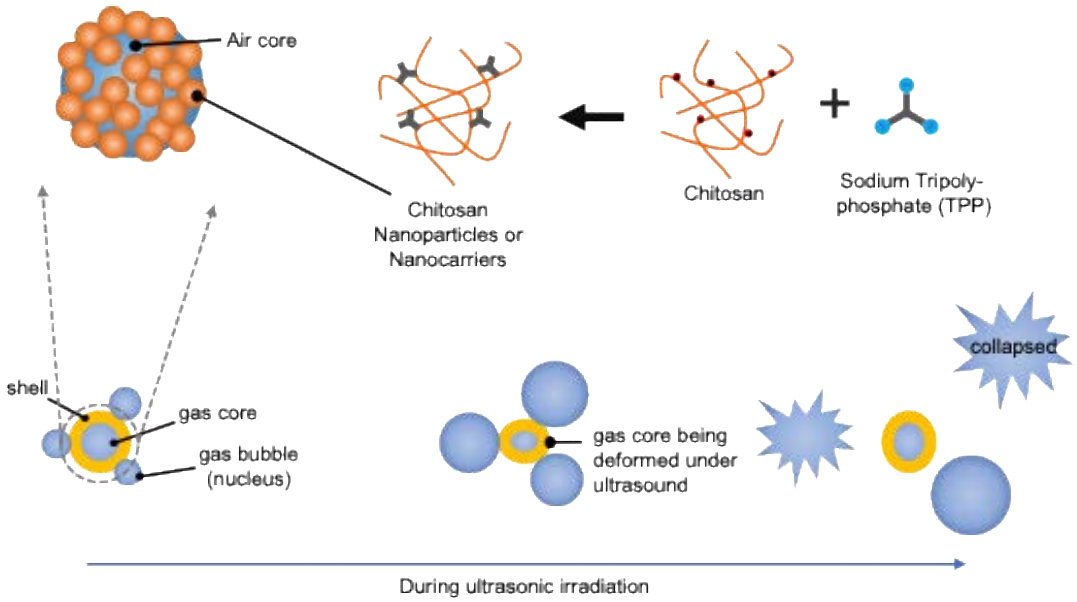

Fig. 1 Schematic illustration of chitosan nanoparticle-shelled composite and ultrasound cavitation associated with the composites in water.

During ultrasound application, the nano-sized air cores undergo low-amplitude sinusoidal radial pulsations, inducing acoustic microstreaming on the surface of the composites. Consequently, gas bubbles (nuclei) attached to the shell begin repetitive growth and shrinkage, accelerated by the deformation of the air core and merging of nanobubbles through acoustic microstreaming. Ultimately, these formed bubbles collapse, generating the cavitation effect, which has the ability to disrupt biological barriers and deliver the drug-loaded carriers (the nanoparticles composing the shell) to targeted sites.

Chapter 2 Chitosan Nanoparticles and Its Ability as Drug Carriers

2.1 Introduction: Theoretical background & Methodology

This chapter discusses chitosan nanoparticles to lay the groundwork for chitosan-based composites. The conditions for chitosan nanoparticle synthesis, size modification techniques, and their functionality as drug delivery carriers are demonstrated. Basic fibroblast growth factor (bFGF, FGF2) is one of the most potent angiogenic growth factors, with a molecular weight of ~18 kDa. bFGF is expressed in many normal adult tissue cells and can regulate the migration and replication of endothelial, epithelial, and fibroblast cells, which are responsible for neovascularization, collagen production, and epithelialization [160]. Because of these roles, supplemental bFGF is essential for healing irradiated postsurgical soft tissue and skin erosion [161]. However, there are challenges in developing adequate systems for such therapeutic proteins to enable their use in daily life, owing to their inherent instability and poor pharmacokinetic properties [162]. In particular, bFGF is easily degraded and has a half-life of a few hours in aqueous solutions or culture media, which limits its use for wound treatment [163]. Therefore, transdermal administration is a candidate method for delivery without the loss of bFGF activity.

Transdermal administration has significant advantages over oral administration owing to the avoidance of the first-pass effect and the harsh gastrointestinal environment and it provides controlled and prolonged drug release [164]. Hence, transdermal administration of bFGF is suitable for the treatment of subcutaneous tissues with the goal of improving subcutaneous tissue activity. However, without being protected by ionic interaction modification [165], chemical modification [166], and physical barriers [167], bFGF in aqueous solutions is degraded by enzymes at the cell surface. Therefore,

methods for the encapsulation of bFGF with carriers have been developed to improve administrative efficiency. However, the stratum corneum (SC), which provides the main protective barrier of the skin, hinders drug permeation [168].

Here is a transdermal drug delivery system enhanced by ultrasound using chitosan nanoparticles as carriers that enable administration over a wide area of the skin [169]. In particular, the transdermal penetration effect of a low-frequency ultrasound-enhanced delivery system using chitosan nanoparticles as the carrier for bFGF was demonstrated in ex vivo experiments on hairless mouse skin. The use of low-frequency ultrasound allows efficient induction of cavitation, which is a factor in penetration by sonophoresis. Fluorescence-labeled chitosan nanoparticles were used to adjust the ultrasound conditions, carboxymethyl chitosan was applied for protein loading, and the validity of the noninvasive delivery system was tested. By rubbing bFGF directly on the skin (Fig. 2a) or applying bFGF contained in nanocarriers to the skin (Fig. 2b), the subcutaneous administration of bFGF was prevented due to the skin barrier. However, the transdermal penetration of bFGF was increased by ultrasound (Fig. 2c), and the transdermal penetration efficiency was further improved using chitosan nanocarriers in combination with ultrasound (Fig. 2d). Therefore, transdermal bFGF delivery improved by ultrasound has demonstrated the capacity of chitosan nanoparticles to load medicines and improve delivery efficiency.

2.1.1 Meterials

Chitosan (low molecular weight, No. 448869, Sigma-Aldrich, USA), sodium tripolyphosphate (TPP, No. 238503, Sigma-Aldrich), acetic acid (No. 64-19-7, FUJIFILM Wako Pure Chemical Corporation, Japan), carboxymethyl chitosan (CMC, DD = 90%, MW = 100-300 kDa, CAS 83512-85-0, Santa Cruz, USA), hydrogen peroxide (30.0%-35.5%, No. 7722-84-1, Sigma-Aldrich), and calcium chloride (anhydrous powder, No. 10043-52-4, Sigma-Aldrich) were used for the synthesis of

chitosan nanoparticles. Recombinant human FGF (No. 4114-TC-01M, R&D Systems, Inc., Minneapolis, MN, USA) was used in the experiments as the model protein. The fibroblast growth factor 2 primary antibody (No. 12115-05041, FITC-conjugated, Assaypro, USA), Alexa Fluor 568 (No. A20003, Thermo Fisher, USA), and Hoechst 33342 (CAS 23491-52-3, FUJIFILM Wako Pure Chemical Corporation) were used to stain the bFGF, chitosan, and cell nuclei, respectively. The extraction buffer for the ELISA method was composed of Trizma hydrochloride solution (pH 7.4, No. T2194, Sigma-Aldrich), Triton X-100 (No. X100, Sigma-Aldrich), and sodium chloride (No. 7647-4-5, Sigma-Aldrich). Phosphate-buffered saline (PBS; No. T900; Takara Bio Inc., Japan), cryofilm (No. C-MK001-C2, cryofilm type 2C (9), Section Lab., USA) and Vector TrueVIEW® autofluorescence quenching kit (No. SP-8400-15, Vector Laboratories, USA) were used in the skin cryosection preparation process.

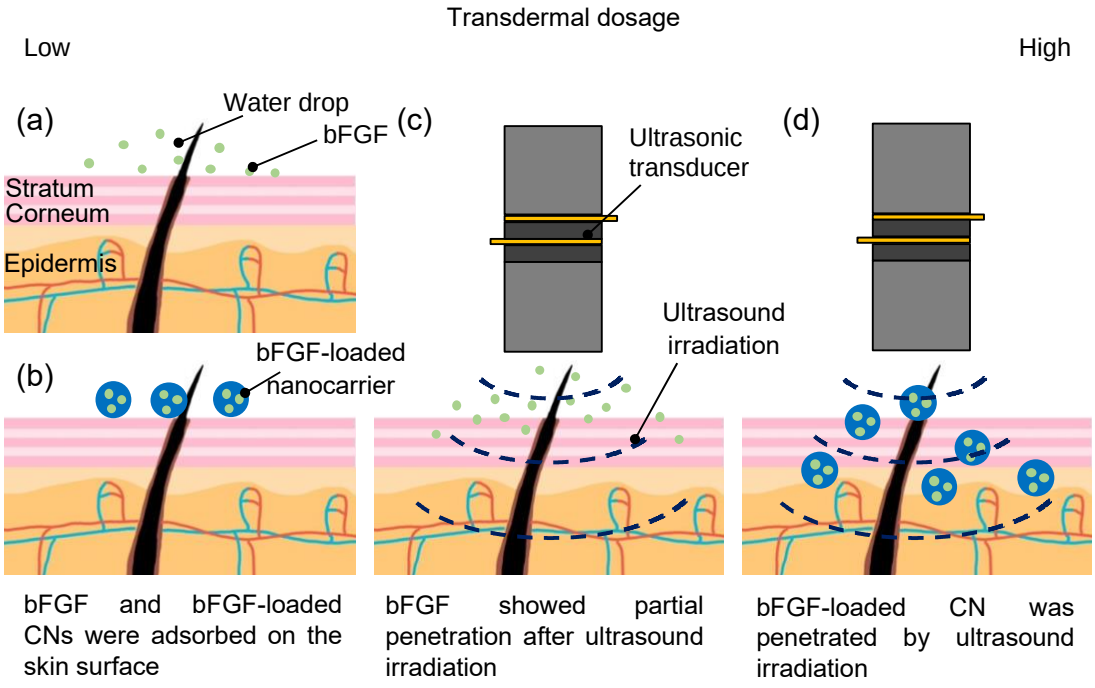

Fig. 2 Concept of transdermal drug delivery of bFGF in our study.
(a, b) A water drop with (a) bFGF or (b) bFGF-loaded carboxymethyl chitosan nanoparticles (CMCNs) was placed on the skin. (c) A water drop with bFGF was irradiated by ultrasound on the skin. (d) Our proposed method: a water drop with bFGF-loaded CMCNs was irradiated by ultrasound on the skin.

2.1.2 Methods

Chitosan powder was dissolved in acetic acid aqueous solutions at various concentrations (0.1~0.2% w/v). TPP powder was dissolved in purified water at different concentrations (0.1~0.2% w/v). Then a variable volume (0.5 - 1.5mL) of TPP aqueous solutions were added into 3 mL of the chitosan aqueous solutions dropwise under magnetic stirring (750-1200 rpm) at room temperature. When the appearance of the mixture is slightly turbid, chitosan nanoparticles (CNs) have formed. Then chitosan nanocarriers were synthesized by dissolving 0.15% (w/v) carboxymethyl chitosan powder in 9.57 mM PBS buffer. Thirty microliters of 30% (v/v) hydrogen peroxide were added to 10 mL of chitosan solution with magnetic stirring and heated for 60 min to synthesize carboxymethyl chitosan nanoparticles (CMCNs) for H_2O_2 degradation. The lid of the mixture was opened and stirred to remove unreacted H_2O_2. Next, 0.8 mL of 5% (w/v) $CaCl_2$ solution was added dropwise to 10 mL of carboxymethyl chitosan solution and stirred for 90 min with magnetic stirring (750–900 rpm) at 25°C. bFGF was added to the carboxymethyl chitosan solution to achieve a protein concentration of 40 μg/mL before the addition of $CaCl_2$. The prepared nanoparticles were stored at 4°C until further use.

The chitosan nanoparticle sizes (CNP or CMCNs) were measured using dynamic light scattering (DLS; SZ-100, Horiba Ltd., Japan). Morphological examination of the chitosan nanoparticle samples was performed using scanning electron microscopy (SEM, S-4800, Hitachi Tech., Japan). The acceleration voltage was set to 5 kV. Measurements of the particle size were performed based on the analysis of 40–100 nanoparticles using several SEM images with ImageJ software. The encapsulation efficiency of bFGF-loaded CMCNs was determined by ultracentrifugation of samples at 15000 × *g* for 30 min at 15°C. The amount of free bFGF in the clear supernatant was measured using UV spectrophotometry at 280 nm [170]. The bFGF encapsulation efficiency was calculated using the following equation:

$$\text{the bFGF encapsulation efficiency}(\%) = \frac{d_{\text{bFGF}}}{d_{\text{CMCNs}}} \times \frac{A_{\text{total}} - A_{\text{unencapsulated}}}{A_{\text{total}}} \times 100,$$

where d_{bFGF} and d_{CMCNs} indicate the densities of bFGF (40 μg/mL) and carboxymethyl chitosan (= 1.5 mg/mL) in the pre-gel solution, respectively. A_{total} and $A_{\text{unencapsulated}}$ indicate the absorbance of the total amount of bFGF and the absorbance of bFGF unencapsulated in CMCNs, respectively.

For quantitative analysis, skin samples were cut using a 12 mm biopsy punch (No. BDYPP1250; Team Medical Supplies, Australia). The skin punches were weighed and homogenized in 1.5 mL of extraction buffer (50 mM Tris pH 7.4, 150 mM NaCl, and 1% Triton X-100) per gram. After homogenization, the tissue lysate was centrifuged at 13000 × *g* for 10 min at 4°C, and the supernatant was stored at –80°C [171]. The skin extracts were diluted 100-fold and used for enzyme-linked immunosorbent assays (ELISA) with a human bFGF ELISA kit (No. P09038, RayBio®), which were performed according to the manufacturer's instructions.

2.2 Characteristics of CMCNs and results of loading efficiency

The next images showed the trend of size change of chitosan nanoparticles by changing the stirring time, adding different amounts of TPP solution or changing the temperature of degradation (Fig. 3). After confirming that the chitosan nanoparticles were capable of penetrating the skin, nanocarriers for bFGF were fabricated using chitosan as the base material. Chitosan particles are generally produced in an acetic acid aqueous solution, but basic bFGF is denatured under acidic conditions in an acetic acid aqueous solution. For neutral synthesis at a pH of ~7 to prevent aggregation and damage to bFGF which has an isoelectric point of 9.6, chitosan nanoparticles were synthesized using carboxymethyl chitosan as the nanocarrier for bFGF. To prepare CMCNs with a

relatively small size for further protein loading, samples were stirred for 18 h after adding 0.8 mL of $CaCl_2$ (aq.), and were degraded by H_2O_2 at 40°C. The diameter of the CMCNs observed by SEM was 72.8 ± 1.1 nm. The primary diameter of the dried CMCNs after protein loading observed in the SEM images was 81.9 ± 1.5 nm.

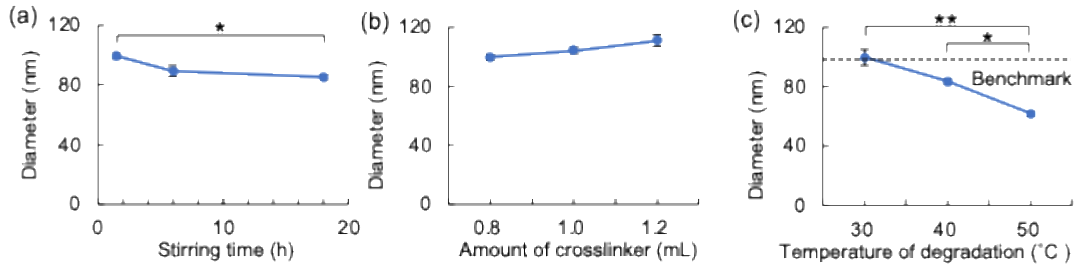

Fig. 3 Synthesized carboxymethyl chitosan nanoparticles (CMCNs) were observed by SEM. (a) The stirring time was changed with a crosslinker amount of 0.8 mL and the reaction temperature of 20°C. (b) The amount of cross-linking was changed with the stirring time of 1.5 h and reaction temperature of 20°C. (c) In addition to the above conditions, the reaction temperature was changed from 30 to 50°C to enable degradation by H_2O_2, with a stirring time of 1.5 h and crosslinker volume of 0.8 mL (n = 40–100, mean ± S.D., *p > 0.05, **p > 0.01, ANOVA). From the above results, CMCNs were prepared by stirring for 18 h, adding 0.8 mL of $CaCl_2$ (aq.), and degradation by H_2O_2 at 40°C.

The CMCNs were loaded by mixing bFGF with aqueous carboxymethyl chitosan during synthesis. The diameter of the bFGF-loaded CMCNs observed by SEM was 81.9 ± 1.5 nm. Therefore, bFGF loading modestly increases the primary diameter. The bFGF-loaded CMCNs had a hydrodynamic diameter of 347.1 ± 3.0 nm as measured by DLS. The CMCNs without bFGF had a hydrodynamic diameter of 239.8 ± 0.9 nm. By comparing the amount of bFGF in the bFGF solution in PBS and bFGF-loaded CMCNs via UV absorption spectrometry, 92.81% of the total bFGF was found to be encapsulated in the CMCNs and the bFGF encapsulation efficiency is equal to 2.47% of the mass of the CMCNs. Subsequently, these bFGF-loaded CMCNs were used to evaluate subcutaneous delivery with bFGF.

2.3 Qualitative & quantitative analysis of protein delivery

To confirm the transdermal penetration of nanocarriers loaded with bFGF on mouse skin using sonophoresis, skin cryosections of hairless mice treated with ultrasound of various vibration amplitudes and synthesized bFGF-loaded CMCNs were observed (Fig. 4a–c). For the control groups, skin tissues were treated using ultrasonic irradiation with nanocarrier-free bFGF (positive control, Fig. 4d) or deionized (DI) water (negative control, Fig. 4e). Ultrasound was applied at a frequency of 45.0 ± 1.0 kHz, with an application time of 5 min and a current of 80–160 mA. The microscopy images of the mouse skin treated with ultrasound and the bFGF-loaded CMCNs (Fig. 4a–c) showed that bFGF (white arrow) penetrated the SC of the hairless mouse skin. bFGF was stuck in the pores (red arrow) of the skin irradiated with carrier-free bFGF. These results suggest that bFGF loading in nanocarriers promotes the transdermal penetration of bFGF by ultrasonic irradiation.

Next, a quantitative analysis using ELISA has been conducted (Fig. 5). The amount of bFGF (= 2.23 ± 0.41 μg/mL) originally contained in the mouse skin was detected as a blank. In the absence of ultrasonic irradiation (= 0 mA), little bFGF was detected beyond that originally contained in the mouse skin with or without the use of nanocarriers (2.13 ± 0.21 and 2.74 ± 0.10 μg/mL, respectively). These results indicate that bFGF attached to the skin surface was removed by the rinsing process, regardless of the presence or absence of the nanocarrier. When ultrasound was applied to mouse skin with bFGF solution (PBS), a higher amount of bFGF (= 5.10 ± 0.48 μg/mL) than blank was detected. This result indicates that bFGF partially penetrated the skin with the help of ultrasonic irradiation. Meanwhile, the bFGF-loaded CMCNs enabled the delivery of a greater amount of bFGF to the mouse skin under ultrasonic irradiation with applied currents of 80 mA (7.20 ± 0.57 μg/mL), 120 mA (7.57 ± 0.71 μg/mL) and 160 mA (7.59 ± 0.61 μg/mL). Based on these results and the fluorescence images of the skin (Fig. 5), bFGF was delivered subcutaneously in large amounts using nanocarriers

with ultrasonic irradiation.

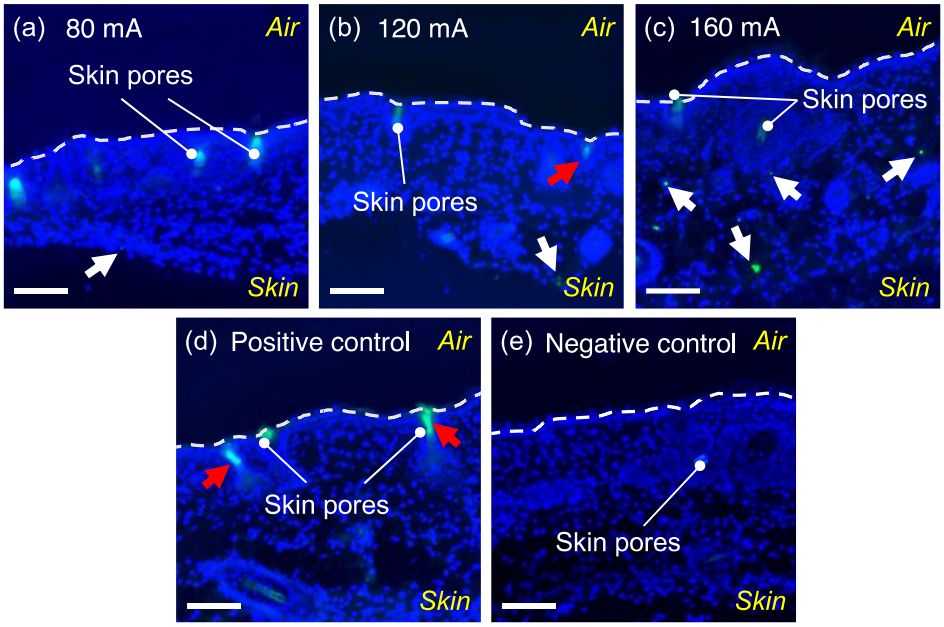

Fig. 4 Microscopy images showing the skin cryosections treated with bFGF. In the fluorescence images, the green, blue, and white dotted lines indicate the FITC-conjugated bFGF, Hoechst 33,342-stained nucleus, and the SC, respectively. The bFGF-loaded CMCNs suspension was used to penetrate the skin by ultrasound with an (a) 80 ± 5 mA, (b) 120 ± 5 mA, and (c) 160 ± 5 mA current applied to the ultrasound transducer. (d) bFGF without CMCNs suspension was used to penetrate the skin using ultrasound with a 120 ± 5 mA current applied to the ultrasound transducer as a positive control. (e) Pure water was used to penetrate the skin using ultrasound with a 120 ± 5 mA current applied to the BL transducer as a negative control. All scale bars = 100 μm.

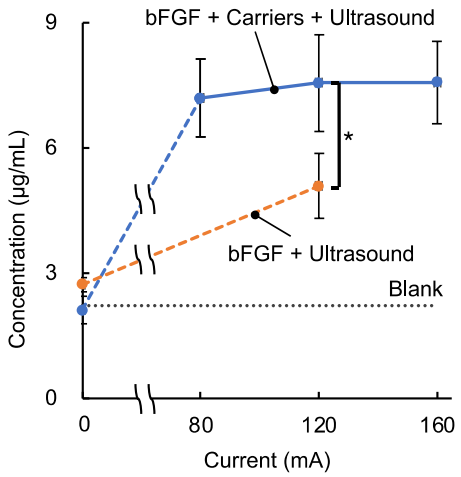

Fig. 5 Quantitative analysis of the amount of bFGF administrated into the skin by ELISA. The amount of bFGF originally present in the skin is shown by the dashed line marked as blank.

Water drops with bFGF and bFGF-loaded CMCNs placed on the skin are shown in the orange and the blue plot, respectively (n = 3, mean ± S.D., *p > 0.05, Student's t-test).

2.4 Summary

By adjusting the amount of crosslinker or its concentration, the size of the chitosan nanoparticle can be controlled from around 20 nm to hundreds of nm. The process of loading proteins into nanoparticles leads to a change in size. The loading efficiency was over 90%. The application of ultrasound and chitosan nanocarriers could lift the concentration of bFGF, while increasing the intensity of ultrasound could lead to better delivery results. It has been shown that carboxymethyl chitosan nanocarriers with the enhancement of ultrasound delivered bFGF into hairless mouse skin *ex vivo*. The primary diameter of the dried CMCNs observed in the SEM images was 81.9 ± 1.5 nm. Under typical low-frequency sonophoresis (LFS) conditions where safety has been confirmed, nanomaterials with a primary diameter of ~100 nm observed by SEM reportedly penetrate the skin [172]. Therefore, the CMCNs synthesized in this study had a size sufficient to penetrate subcutaneously using ultrasonic irradiation.

The enhancement in the presence of chitosan nanocarriers was thought to be attributed to the acoustic cavitation effect, which disrupt the skin barrier and leave channels for drug carriers to entry. The ability of chitosan nanoparticles to load proteins has been proven. Therefore, even if the composites are destroyed under ultrasonic irradiation, the drug-carriers can still finish their task. Sonophoresis uses ultrasound to disrupt the structure of the SC, enabling a transdermal delivery route for macromolecules which has shown promising results in delivering heparin, insulin, and other peptides [173]. Sonophoresis with these drugs has been actively studied because the relatively low-molecular-weight drugs (< 10,000 Da) can easily penetrate the skin when assisted by sonophoresis. Meanwhile, the transdermal penetration of relatively large nanomedicines (tens to hundreds of nanometers) is difficult because ultrasonic

irradiation conditions will require optimization [172,174,175]. Therefore, conventional studies have focused on the size of drugs transdermally delivered by sonophoresis alone. However, the results showed that contrary to previous studies, the use of nanocarriers of increased size improved the efficiency of bFGF administration in combination with sonophoresis. The results indicate that the protection provided by easily degradable nanomedicine and the effect on acoustic cavitation from the additives may affect the performance of sonophoresis. Therefore, in the next chapter, we focused on designing chitosan nanoparticle-shelled composites, which could be promising for various applications due to their ability to enhance the acoustic cavitation effect.

Chapter 3 Size and Structural Analysis of Chitosan Nanoparticle-Shelled Composites

3.1 Introduction: Theoretical background & Methodology

Microbubbles are defined as gas-filled bubbles with diameters in the micron range, and can enhance ultrasound contrast and act as a vehicle for drug delivery [16]. Microbubbles can be classified based on their shell materials, including lipid, protein, and polymeric microbubbles. Lipid microbubbles are biocompatible, but they are prone to gas diffusion and collapse [126]. Protein microbubbles, typically using albumin, provide stability but may have immunogenicity concerns [127,128]. Polymeric microbubbles can offer greater stability and tunable properties but normally involve more complex synthesis processes. Some experiments have shown that microbubbles can be formed by attaching a shell material to the surface of particles, followed by dissolution of the particle core, creating a microbubble structure. [129,130]. In Chapter 2 the ability of chitosan nanoparticles to load proteins has been proven. Due to acoustic cavitation, these chitosan nanoparticles have successfully delivered proteins into the skin samples of hairless mice. Moreover, in this chapter, chitosan nanoparticle-shelled composites were prepared using a simple emulsification process. This process involves mixing anionic surfactants with cationic nanoparticles, which allows for efficient, scalable production under mild conditions. The goal is to enhance the acoustic cavitation effect and expand its potential applications.

Chitosan microbubbles have emerged as a promising tool in the field of therapeutics due to their unique properties and multifunctional capabilities. The advantages of chitosan microbubbles come from their unique combination of chitosan and microbubbles. These include biocompatibility, biodegradability, targeted delivery with minimal side effects, and their impact on ultrasonic mechanisms due to their structure.

The goal of the experiment is to design a composite that is effective in enhancing acoustic cavitation, which is promising in drug delivery and sonochemical reaction inception. Nanobubbles with chitosan as the shell have not been widely studied, which perhaps is due to the application of chitosan focusing on drug carriers. In this chapter experimental results about the synthesis of chitosan nanoparticle-shelled composites were shown by adjusting time, shaking speed, the volume ratio of chitosan nanoparticles to SDS and mixing methods. Electron microscopy and optical microscopy were applied to observe the composites.

CNP-shelled composites were prepared by shaking mixtures containing 100–500 μL of a stock CNP solution and 100–400 μL of 10 mM SDS solution for 5–120 min. Purified water was added to ensure a total liquid volume of 700 μL. Shaking was performed at various speeds using a thermoshaker (TS-100C, Biosan, Latvia), with the optimized speed determined to be 1200 rpm. CNPs with different sizes have been applied to synthesize composites. The hydrodynamic size and zeta potential of CNPs were measured using a nanoparticle analyzer (nanoPartica SZ-100V2, Horiba Ltd., Japan). For each chitosan nanoparticle formulation, based on the same concentration and ratio, three independent samples were synthesized, and the hydrodynamic size measurements were performed three times on each of the three samples. The mean size and standard deviation were calculated from the results of these three samples (n = 3, where n represents the number of experimental repetitions), ensuring the reliability of the data. Composite samples were diluted 50-fold, and 10 μL of each solution was placed onto an ultra-flat silicon wafer, allowing the solvent to evaporate for scanning electron microscopy (SEM, S-4800, Hitachi High-Tech Co., Japan). SEM imaging was conducted with an acceleration voltage of 5 kV. Purified water was used as the dilution medium. Ultrasound irradiation was applied by a homogenizer (20 kHz) with a duty cycle of 75%. All the Eppendorf tubes filled with composite samples can be set around the ultrasound transducer in the water bath to keep them at room temperature. The

distance of a certain tube to the transducer was set to the same by a microtube floating rack. Also, the homogenizer was directly applied to samples of 20 mL without a water bath and a disposable centrifuge tube as the container.

3.2 Hydrodynamic size of chitosan nanoparticles and photographs

The next figure showed the trend of hydrodynamic size of chitosan nanoparticles (Fig. 6). The chitosan nanoparticle synthesized with a lower concentration of TPP solution has a size of 26.18±5.76 nm and the nanoparticle with a higher concentration has a size of 34.45±1.49 nm. The result demonstrated that even though the total mass of chitosan and TPP was the same, the concentration could still affect the particle size. Besides, chitosan nanoparticles in 1 mL of 0.2% w/v TPP solution have agglomerated and thus cannot be measured by DLS. Although the chitosan nanoparticle has the appropriate size, the relatively low concentration may affect further experimental steps. Chitosan nanoparticles prepared by adding 500 μL of 0.2% w/v TPP solution into 0.15% w/v chitosan solution followed by adding 300 μL of pure water or not have sizes of 24.25 nm or 25.42 nm, which may prove that adding water after adding TPP might not affect the size. Besides, using a high-concentration TPP solution seems to lead to higher deviations in the measuring results, which means the formation of nanoparticles under high concentrations may not be stable or have more agglomeration. Based on these results, the following conditions were selected for synthesizing CNPs for use in composites: chitosan concentration 0.15% w/v, TPP concentration 0.20% w/v, and TPP volume 500 μL.

For further experiments, the volumes of chitosan and TPP solutions were scaled up to 15 mL and 2500 μL, respectively, while maintaining the same chitosan and TPP concentrations. The size trend after scaling up, shown in Fig. 7, was similar to that observed in Fig. 6 for lower volumes of chitosan and TPP solutions. The sizes of

chitosan nanoparticles were altered by tuning the volume of TPP solution. The added amounts of TPP solution were 2.5, 3.2, 3.5, 3.7, 4.0, 4.2, and 4.5 mL, respectively. The sizes of chitosan nanoparticles were 22.60, 27.20, 28.87, 32.73, 38.13, 42.07, and 55.91 nm when the amounts of TPP were 2.5, 3.2, 3.5, 3.7, 4.0, 4.2, and 4.5 mL, respectively. The average hydrodynamic size of the CNPs used in composite formation was 22.6 ± 2.6 nm, obtained when the volume of TPP solution was 2.5 mL, based on 10 measurements of 3 samples. The zeta potential of the nanoparticles, measured 10 times, was +58.5 ± 1.0 mV.

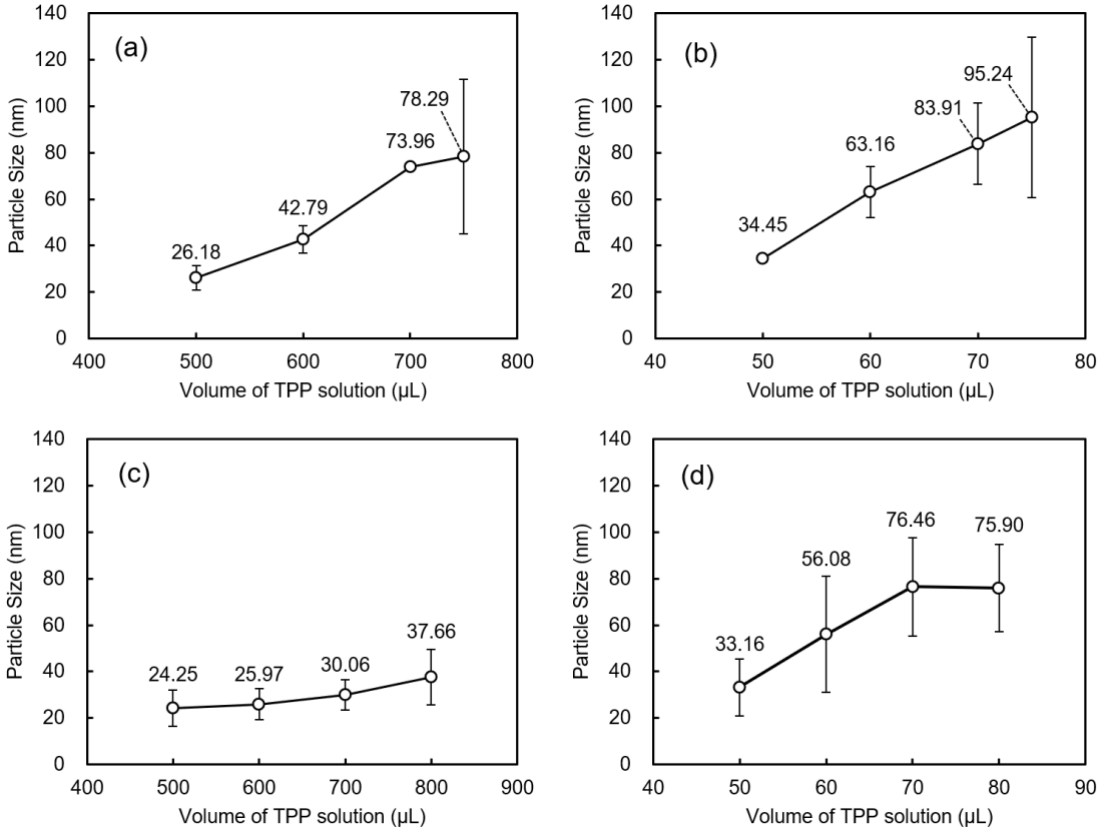

Fig. 6 Dependence of the hydrodynamic size of chitosan nanoparticles on chitosan concentration, TPP concentration, and volume of TPP solution.

The hydrodynamic size of chitosan nanoparticles was evaluated using the dynamic light scattering method (n = 3, mean ± standard deviation). The chitosan solution concentrations are 0.10 % w/v for (a) and (b), and 0.15 % w/v for (c) and (d). The TPP solution concentrations are 0.2 % w/v for (a) and (c), and 2.0 % w/v for (b) and (d). The numbers in the figure represent the hydrodynamic sizes of the nanoparticles in nanometers (nm). n represents the number of experimental repetitions.

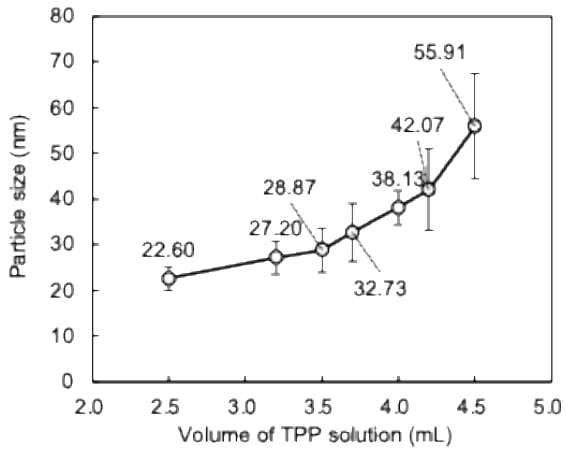

Fig. 7 Dependence of the hydrodynamic size of chitosan nanoparticles on the volume of TPP solution. The hydrodynamic size of chitosan nanoparticles was evaluated using the dynamic light scattering method. The concentration of the chitosan solution is 0.15% w/v, and the concentration of the TPP solution is 0.2% w/v. The numbers in the figure represent the hydrodynamic sizes of the nanoparticles in nanometers (nm). (n = 3, mean ± S.D. n represents the number of experimental repetitions.)

3.3 Morphological characterization of optical and electrical microscopes

CNP-shelled nanobubbles and the original chitosan nanoparticle have been observed by SEM. The dilution factor and the amount of solutions were set to the same so the SEM images may be compared. The following images are some of the SEM images (Figs. 8 & 9). When being shaken for 1~5 minutes, the mixture did not seem to show much difference but just nanoparticle agglomeration. When the shaking speed was too slow, there seemed to be no nanobubbles but just particle agglomerations, which may be due to the gas bubbles that played as the core of the nanobubbles being too small at low speeds. When raising the shaking time to 30 minutes or 2 hours, there seems to be a hollow region in the particles (Fig. 8), which may be the proof of gas cores.

With a short shaking time, the sample does not appear to be significantly different in morphology from pure chitosan particles (Fig. 9a). While shaking the mixture with the same composition for a longer time like 30 minutes, there seemed to be some circle-like distributions (Fig. 9a), which was not quite clear due to the low volume ratio of

CNPs to SDS. The ratio in Fig. 9a was 0.5:1 and the shaking speed was 1200 rpm by a thermoshaker. Increasing the ratio did not create a significant difference between the sizes of the composites but only made them a little bit larger, which were all around 1 μm (Fig. 9b). Moreover, lengthening the stirring time, raising the ratio of CNPs to SDS, or reducing the speed seemed to be responsible for the increased composite sizes. Decreasing the shaking speed to 750 rpm and reducing the shaking time to 5 minutes seemed to be helpful in preparing composites with small sizes (Fig. 9b). Chitosan nanoparticles used in figures 8 and 9a and b have a size of 22.6 nm. By changing the size of CNPs, it can be seen that some images do not have a clean background and the chitosan nanoparticles have agglomerated to some level (Fig. 9c). Compared with previous results, there seemed to be no significant difference between the sizes of the composites, which were all around 1 μm. However, the thickness of the composites may be affected by the size of the CNPs.

Though the composite is transparent making it not easy to observe, some of the photos indicated there may be a sphere-like shape and some photos seemed to show nanobubbles with a gas core inside (Fig. 10). Figure 10 shows several composite samples under an optical microscope that were prepared by the same chitosan nanoparticles with a size of 22.6 nm but added in different amounts. Tiny bubbles with a gas core and chitosan nanoparticle clumps coexist in these images. Besides, raising the amount of SDS seems to be meaningful in reducing the agglomeration of chitosan nanoparticles. Chitosan nanoparticle-shelled composites prepared by using different chitosan nanoparticles have also been observed under an optical microscope. Many images also showed the presence of bubbles (Fig. 10). However, due to the limitation of the magnification of the optical microscope, clearer images were not obtained. Further confirmation of the presence of gas cores and the size measurement of composites may require SEM observations.

To prepare CNP-shelled composites, longer shaking times and higher volume ratios between CNP suspension and SDS solution are preferable. This is because longer shaking times provide sufficient energy for the migration and deposition of CNPs at the gas-core interface, ensuring the formation of a stable and complete shell structure. Insufficient shaking time leads to incomplete coverage and instability of the composites, as observed in Figs. 8 and 9. A higher volume ratio of CNP suspension provides more CNPs, which are essential for stabilizing the gas core. However, no clear morphological difference was observed in the composites with increased amounts of CNPs, as shown in Fig. 9b, suggesting the following formation mechanism. The emulsification process influences the size of the gas core; however, as the concentration of surfactant (SDS) controls the emulsification, the size of the gas core likely remained unchanged under a constant SDS concentration. No coagulation of CNPs on the core was observed, even with larger amounts of CNP suspension, because the deposition of CNPs on the gas core is regulated by the interfacial effect between the SDS covering the gas core and the CNPs.

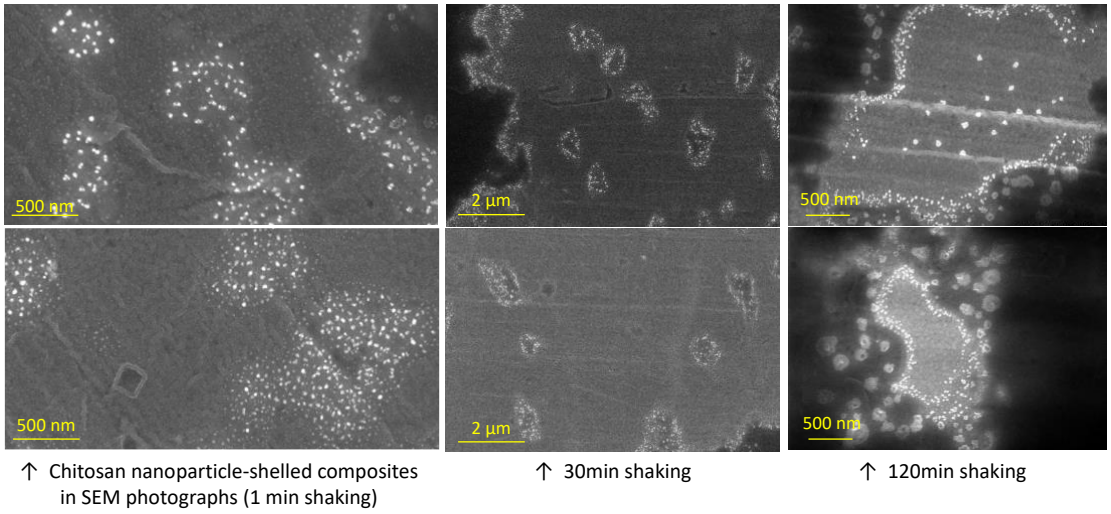

Fig. 8 SEM images of CNP-shelled composites with altering the shaking time during composite preparation. The scale bars are on the images. The shaking times for the left two images are 1 min, the middle two images are 30 min, and the right two images are 120 min.

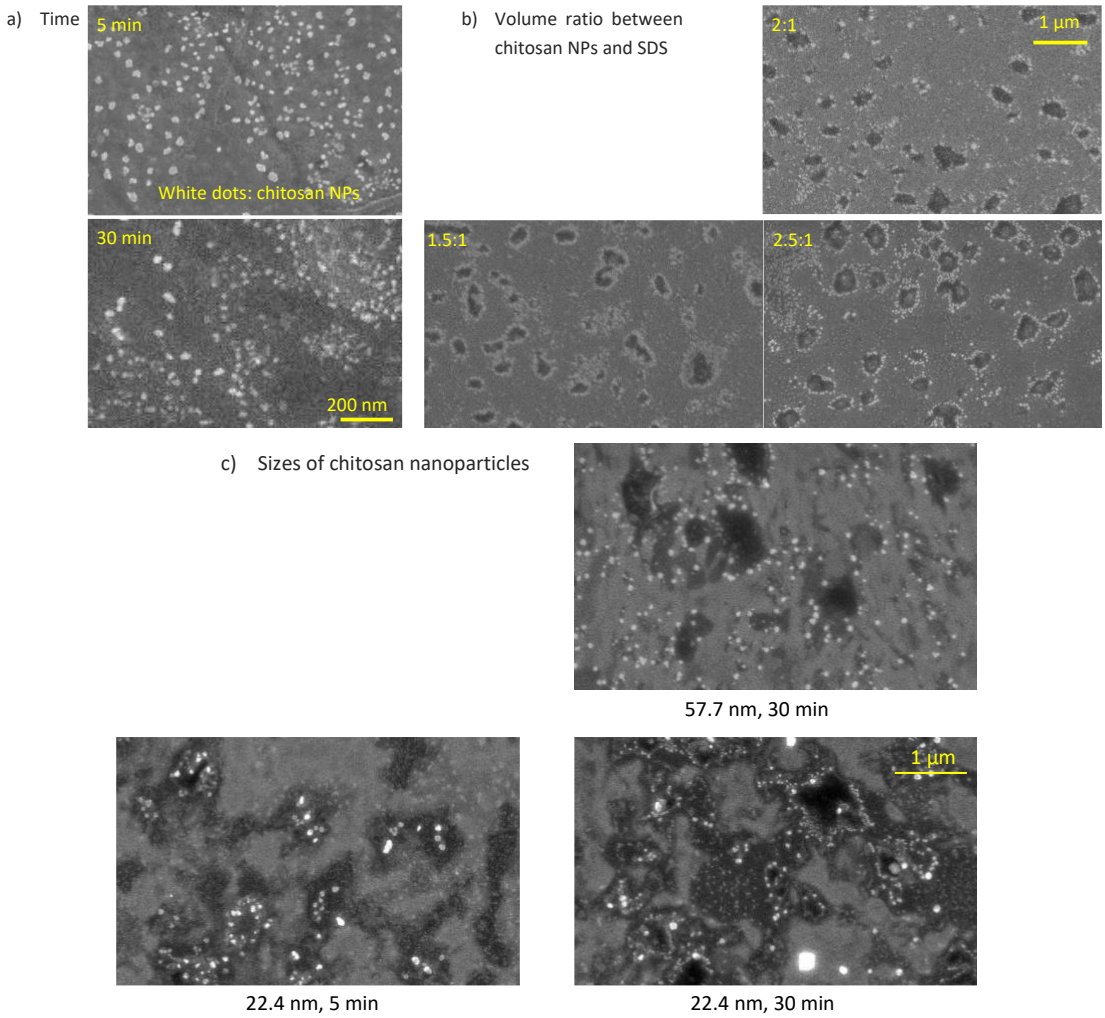

Fig. 9 SEM images of CNP-shelled composites with altering the shaking time (a), the volume ratio between CNPs and SDS (b) or the size of chitosan nanoparticles (c) during composite preparation. The scale bars are on the images.

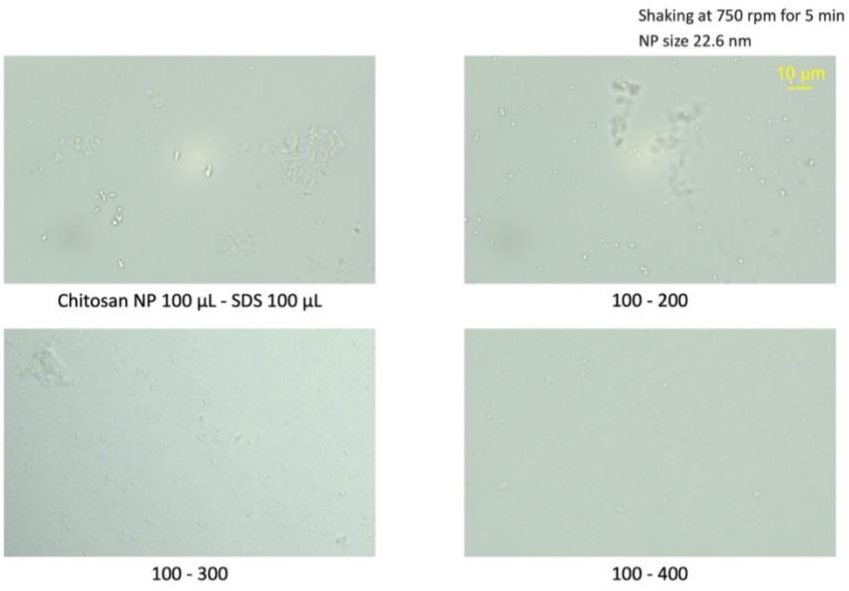

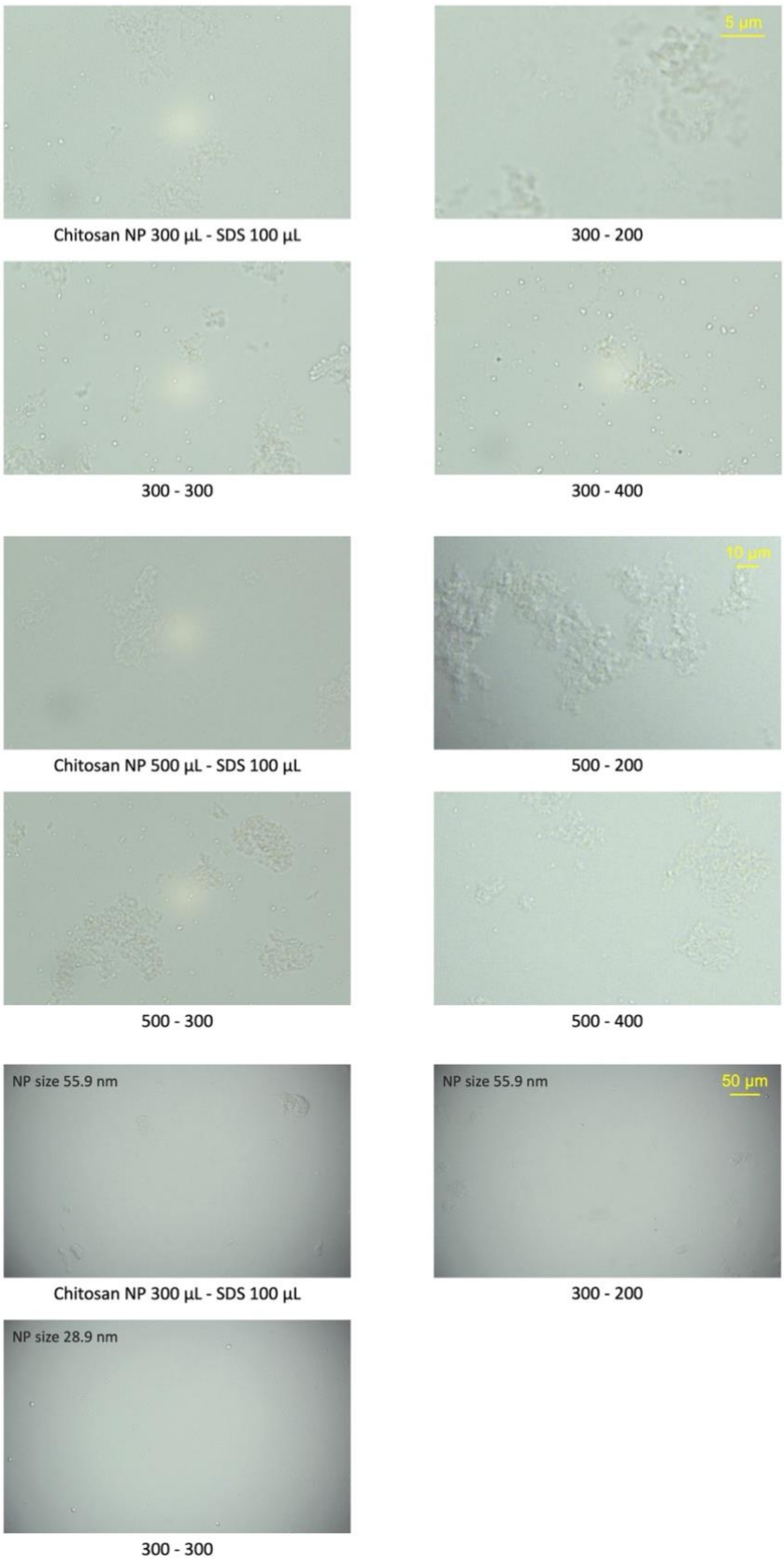

Fig. 10 CNP-shelled composites prepared by several CNPs at different ratios between CNPs and SDS by an optical microscope (Shaking at 750 rpm for 5 min).

3.4 Summary

Particle size increased with the increasing amount of crosslinker; however, the zeta potential decreased slowly. Optical photographs showed that CNPs with a low concentration may be helpful in preparing nanocomposites with a gas core. However, due to the limitations of the optical microscope's magnification, clearer images were not obtained. Further confirmation of the presence of gas cores and size measurement of the composites was conducted by SEM observations. As the shaking time lengthened or the volume ratio between CNPs and SDS increased, the size of the composites seemed to increase. The ratio between SDS and nanoparticles may need to be adjusted to prepare smaller composites. However, measuring the size of the composites precisely remains a problem. The performance of CNP-shelled composites is evaluated in the next section using iodide dosimetry and terephthalic acid dosimetry.

Chapter 4 Analysis of Acoustic Cavitation Enhancement by Chitosan Nanoparticle-Shelled Composites

4.1 Introduction: Theoretical background & Methodology

Chitosan nanoparticle-shelled composites have been prepared while altering the shaking time, shaking speed, or volume ratio between chitosan nanoparticles and SDS solution in Chapter 3. The morphology check has been conducted using optical and electrical microscope photographs, which could act as direct evidence to prove the presence of gas cores therefore the structure of microbubbles. Assessing the effect on ultrasound acoustic cavitation by iodide dosimetry and terephthalic acid dosimetry became the main point of this chapter, which could demonstrate the promise of the proposed composite and act as indirect evidence of the presence of the gas cores.

4.1.1 Iodide dosimetry

When water is sonicated, the adiabatic collapse of cavitation bubbles leads to the formation of radical species, such as hydroxyl radicals (•OH), hydrogen peroxide (H_2O_2) and hydroperoxyl radicals (HOO•) [176]. There are numerous ways to measure and determine inertial cavitation. Chemical products can be utilized to quantify cavitation activity since cavitation effects include both mechanical and chemical impacts [177]. The chemical implications of inertial cavitation can be observed using iodide dosimeters, terephthalate dosimeters, and Fricke dosimeters, among other chemical approaches [176,178]. Iodide dosimeters and Fricke dosimeters, which are photometry-based dosimeters, are not very sensitive. Iodide dosimeters, however, are relatively easy to use and universally accepted. The iodine dosimeter yields consistent and repeatable findings, but it lacks the sensitivity needed for some sonochemical applications. It is commonly accepted that the oxidation of potassium iodide (KI) serves as a reference for calibrating sonochemical efficiency. Furthermore, handling and preparing KI

solutions are straightforward.

Iodine ions in KI aqueous solution can change into iodine molecules when exposed to ultrasonic radiation, which is the basis for the KI dosimetry method's calculation of cavitation activity [179]. Thus, the acoustic cavitation can be measured using the iodine release. When ultrasound is applied to a potassium iodide (KI) aqueous solution, oxidation occurs and I^- ions are oxidized by the generated radicals to give I_2. The excess of I^- ions present in solution react with I_2 to form I_3^-. The amounts of I_3^- ions can be quantified by a UV spectrophotometer at 350 nm. The main reactions occurring with this method are shown below:

$$H_2O + \text{ultrasound} \longrightarrow \cdot H + \cdot OH$$
$$\cdot OH + I^- \longrightarrow OH^- + I_2$$
$$I^- + I_2 \rightleftharpoons I_3^-$$

The KI dosimetry method was utilized to assess the enhancement effect of ultrasound with NaI solutions (100 mM) in these experiments. Sodium iodide was added before ultrasound irradiation, and the ultrasound is applied for up to 120 minutes. Iodide solution, iodide solution with added SDS, iodide solution with added chitosan nanoparticles and iodide solution with added chitosan composite were subjected to ultrasonic treatment. After ultrasonic treatment, the sample was subjected to centrifugation at 15000 rpm for 30 minutes twice to collect the supernatant (Model 3700, Kubota Co., Ltd, Japan). The absorbance of I_3^- (355 nm) was measured by UV-visible spectroscopy (BioSpec-nano, Shimadzu Corporation, Japan).

4.1.2 Terephthalic acid dosimetry

Moreover, studies have demonstrated that terephthalic acid (TA) is useful for measuring and identifying free hydroxyl radicals produced when cavitation bubbles collapse in ultrasonic fields. 2-hydroxyterephthalate ions, which are very fluorescent, are produced when the terephthalate ions combine with hydroxyl radicals [180,181]. An established technique for tracking acoustic cavitation is terephthalic acid dosimetry, although it

requires a spectrofluorometer and is time-consuming. Besides, PB buffer is widely used in TA dosimetry as it plays a crucial role in maintaining pH stability during the reaction, which could potentially affect the stability of chitosan nanoparticles.

Terephthalic acid (TA, 2 mM, 0.033 g) was dissolved by heating (water bath at 80°C), then 0.02 g of NaOH and TA were dissolved in 100 mL of PB solution (pH = 7.4, prepared from KH_2PO_4 <0.58 g> and Na_2HPO_4 <0.98 g> then dilute 10 times). Before use, the solution was kept in the refrigerator (around 4°C) and in the dark to prevent a photochemical reaction. Chitosan nanoparticle-shelled composites were prepared by shaking the mixture containing 200 - 1000 μL of a stock solution of CNPs and 200 - 600 μL of 10 mM SDS solution at 1200 rpm for 30 minutes (purified water was added to meet the same total liquid volume, which was 1400 μL). 15 Eppendorf tubes were simultaneously shaken using a thermoshaker, followed by combining them for ultrasound irradiation. Then the composites were washed twice with PB solution for further terephthalic acid dosimetry. After the washing process, the precipitation (composite) was combined with 5 mL of solution medium and added to 15 mL of the TA solution, ready for ultrasonic treatment. Purified water, TA solution, and TA solution with added chitosan composite were subjected to ultrasonic treatment. The ultrasonic treatment was conducted using a homogenizer at room temperature for 60 minutes, utilizing a disposable centrifuge tube as the container (frequency: 20 ± 1 kHz, output: 10%, device: UX-300, Mitsui Electric, Japan). The output was set to 10% for composite-involved ultrasound treatment experiments. The fluorescence intensity was measured using a spectrofluorometer (F-7000, Hitachi High-Tech, Japan, excitation wavelength: 315 nm, emission range: 350–550 nm, scan speed: 240 nm/min, excitation slit: 10 nm, emission slit: 10 nm, photomultiplier voltage: 400 V).

4.2 Results of KI dosimetry and issues

Several kinds of CNP-shelled nanocomposites synthesized by adjusting the volume ratio between SDS and chitosan nanoparticles were tested by KI dosimetry. Figure 11 shows the absorbance results of I_3^-. The shaking speed during composite synthesis was altered to 250, 500, 750 or 1200 rpm (Figs. 11 and 12). The volume ratio between chitosan nanoparticles and SDS solution was altered during the composite synthesis, to prepare different composite samples. The values of the absorbance were relatively low, which may be attributed to the unclear trend of the effect of the ratio between chitosan nanoparticles and SDS. It seems to be that composites synthesized at 1200 rpm had better performance on ultrasound enhancement, which may be because of the different sizes of composites and more air bubbles being introduced into the mixture.

In Fig. 13, the conditions for synthesizing these composite samples were shaken by a thermoshaker for 30 minutes at 1200 rpm. The concentration of sodium iodide was 0.1 or 1 M. The ultrasonic irradiation was applied by the homogenizer for 120 minutes with a water bath to keep the temperature at 22°C, or lower than 40°C without a water bath. In Fig. 13a and 13c, the volume of CNP was fixed at 100 μL while the quantity of SDS was varied. In Fig. 13b and 13d, the volume of SDS solution was fixed at 200 μL while the quantity of CNP was altered. In Fig. 13a and 13b, sodium iodide solution was used as a benchmark, and the solution was heated to 60°C for 2 h on a hot plate. In Fig. 13c and 13d, the sodium iodide solution was subjected to ultrasonic irradiation under the same conditions as the composite samples. Compared with NaI solutions heated at 60 degrees for 2 hours, all ultrasound-irradiated samples have shown higher absorbance values, which indicates that a water bath may not be necessary since the effect of heating during ultrasonic irradiation was not outstanding (Figs. 13A and 13B), which is consistent with the conclusion that the solution temperature showed restricted influence on potassium iodide oxidation by some researchers [176]. The trend of the effect of the ratio between chitosan nanoparticles and SDS was still unclear. The

absorbance in Fig. 13c and 13d was relatively lower than that in Fig. 13a and 13b, likely due to the change in sodium iodide concentration.

Compared with either heated or irradiated sodium iodide solutions, all CNP-shelled composites demonstrated higher absorbance, indicating an increased chemical reaction rate in the presence of the composites. In Fig. 13c and 13d, an orange dotted line represents the SDS solution after 2 h of ultrasound irradiation, which consisted of 200 μL of SDS solution and 0.1 M sodium iodide. Based on the absorbance in Fig. 13c and 13d, the SDS benchmark showed a 1.12-fold improvement over the decomposition of ultrasonically treated sodium iodide solution. The use of composites resulted in improvements in hydroxyl radical generation ranging from 1.73-fold to 1.98-fold, outperforming SDS by 54% to 77%, respectively, suggesting that the generation of acoustic cavitation is enhanced.

During the ultrasonic treatment of the potassium iodide solution with added chitosan composite, the homogenizer sometimes stopped working due to excessive foam, which might be caused by the reduced total liquid volume or the acoustic cavitation growth during the irradiation. It can be seen that with the addition of chitosan nanoparticles or composites, the spectra showed higher peak absorbance values than the values of KI and SDS samples (Figs. 13C and 13D).

To summarize here, for different shaking speeds, it seemed to be that composites synthesized at 1200 rpm had better performance on ultrasound enhancement. A water bath may not be necessary during ultrasound application by the homogenizer since the effect of heating is not outstanding. Further experiments were conducted with a NaI concentration of 100 mM since at a lower concentration the difference between ultrasound-applied and non-applied samples was clearly enough. It seemed that the enhancement of ultrasound by composites was confirmed, while the effect of changing

the ratio of chitosan nanoparticles and SDS remained unclear.

In the iodide dosimetry method, the determination of cavitation activity is based on the fact that iodine ions in KI aqueous solution can be transformed into iodine molecules under ultrasonic irradiation. In previous results, it can be seen that with the addition of chitosan nanoparticles or composites, the spectra have shown higher absorbance peak values than the values of KI and SDS samples. Chitosan would form complexes with iodine and the purple coloring of the complexes is primarily I_3^- ions, which can be seen in the sample photo (Fig. 14). Thus precise quantitative measurements of the degree of cavitation activities would be hard to achieve without any additional method to hinder the formation of chitosan-iodine complexes. Moving forward, TA dosimetry was applied to avoid this issue and obtain a precise quantitative analysis of the ultrasound acoustic cavitation effect.

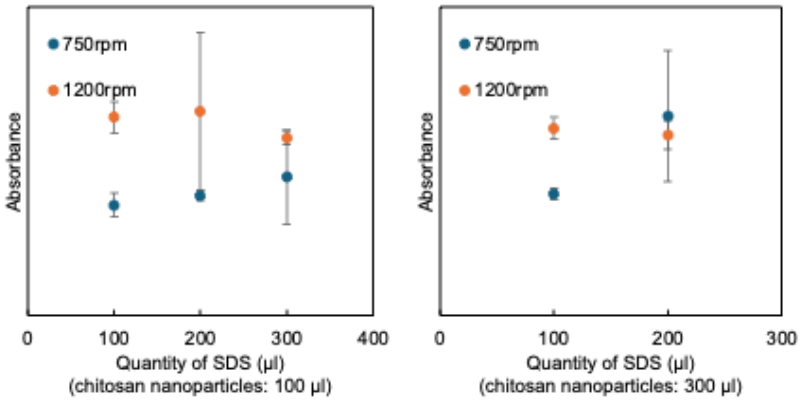

Fig. 11 Absorbance of I_3^- measured by UV-vis spectroscopy on different composite samples. The composite samples were prepared while changing the shaking speed (750 or 1200 rpm). The concentration of sodium iodide was 0.1 M. The treatment time of ultrasound was 60 min. (n = 3, mean ±S.D.)

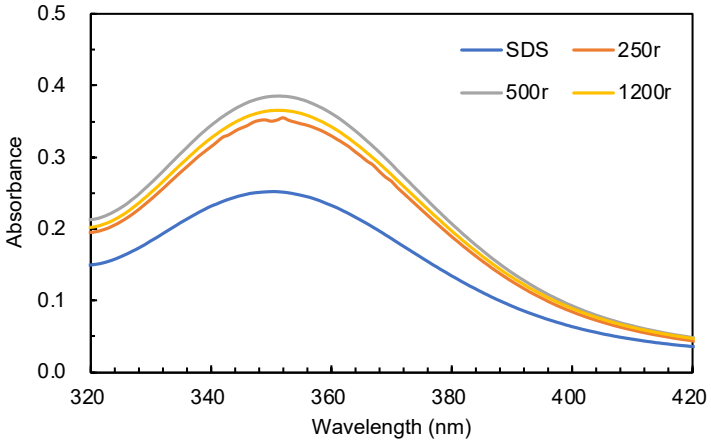

Fig. 12 Absorbance of I_3^- measured by UV-vis spectroscopy on different composite samples and SDS solution. The concentration of sodium iodide was 0.1 M. The treatment time of ultrasound was 60 min. The volume ratio between CNP and SDS was 1:2. The composite samples were prepared while changing the shaking speed (250, 500 or 1200 rpm). (n = 3, mean ±S.D.)

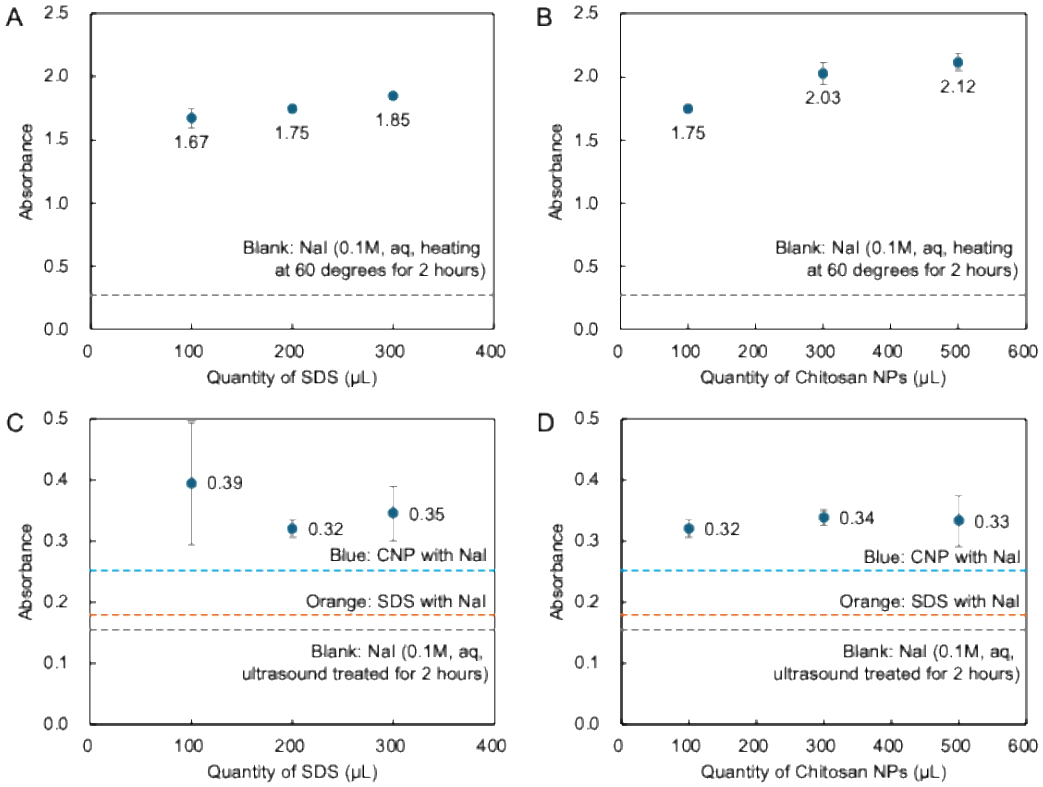

Fig. 13 Absorbance of I_3^- measured by UV-vis spectroscopy on different irradiated composite samples: Concentration of sodium iodide (A and B) = 1 M, (C and D) = 0.1 M. (A) and (C) showed the absorbance change during the quantity of SDS increasing when CNPs was 100 μL. (B) and (D) showed the absorbance change during the quantity of CNPs increasing when SDS was 100 μL. The benchmark is sodium iodide solution that was either heated or treated with ultrasound, represented by dashed lines in each graph. (n = 3, mean ±S.D., *$p < 0.05$, Student's t-test)

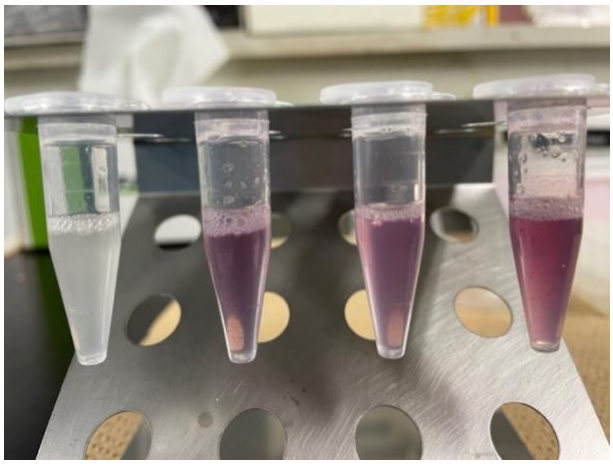

Fig. 14 Purple coloring of the chitosan-iodine complexes after ultrasound treatment.

4.3 Results of TA dosimetry

The following figure (Fig. 15) shows the fluorescent intensity peak values of ultrasonic-treated TA solutions added with chitosan composites. The ratio between chitosan nanoparticles and SDS has been altered and the ultrasonic treatment time was 10 - 60 minutes. To analyze the impact of ultrasonic treatment on TA decomposition, the treatment time was set at intervals of 10 minutes. Labels such as "CNP1SDS1" signify a 1:1 ratio between chitosan and SDS, as with the other labels. After widening the slit width in the measuring conditions to 10 nm in the fluorescence spectroscopy, the curves now exhibit smoother peaks, allowing for better differentiation among various composite samples. PB buffer was utilized as the solvent for the TA solution and for washing composite samples before ultrasonic irradiation experiments. Given that PB buffer has a simpler composition and a lower concentration of salt ions, it is anticipated to enhance the stability of chitosan composites and nanoparticles compared to PBS buffer. Moreover, adjusting the pH of PB buffer is more convenient than using purchased PBS tablets. The pH values of both the TA solution and the TA mixed solution, with added chitosan composites, were measured before ultrasonic treatment, and the results are presented in the table below (Table 1). Notably, the pH values show minimal variation, which is reasonable due to the buffering effect. Subsequent TA

dosimetry experiments were conducted with TA solution in PB buffer.

Table 1　pH values of part of the samples before ultrasonic irradiation.

	TA	TA and CNP1SDS1	TA and CNP1SDS3	TA and CNP3SDS2
pH	7.21	7.23	6.97	7.02

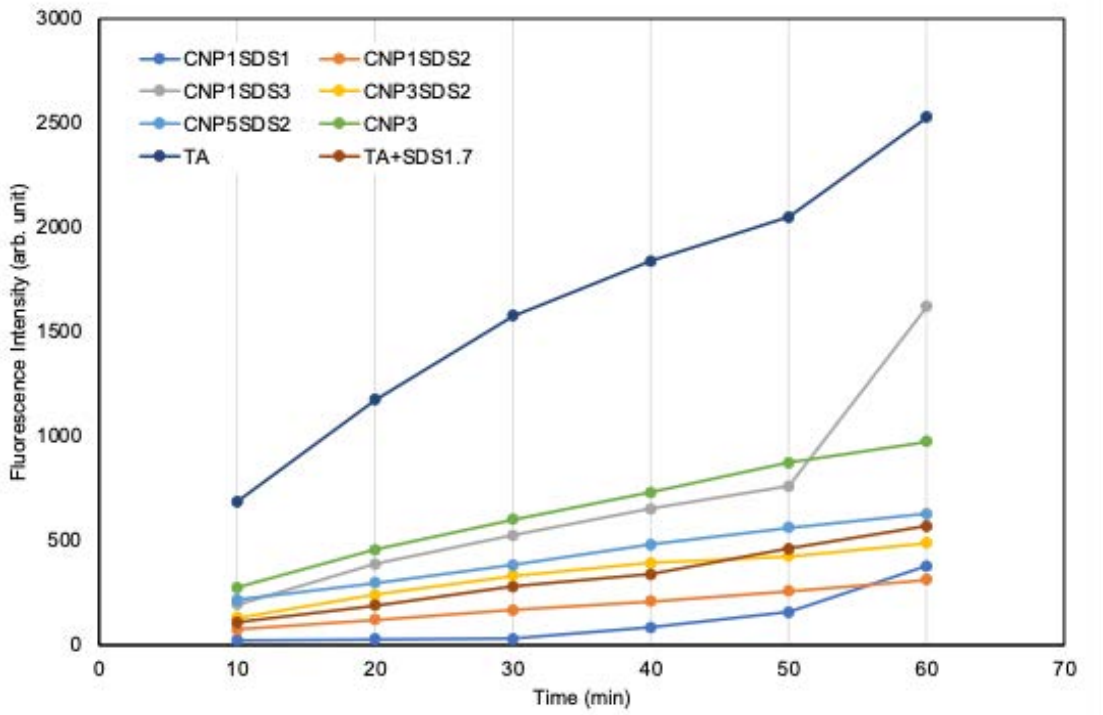

Fig. 15　Fluorescence intensity peak values of TA dosimetry at 425 nm while different composite samples and TA solutions have been measured.

The label of sample's name indicated the volume ratio between CNP and SDS. The treatment time of ultrasound was set at intervals of 10 minutes (Ex: 315 nm, Em: 425nm. n =1).

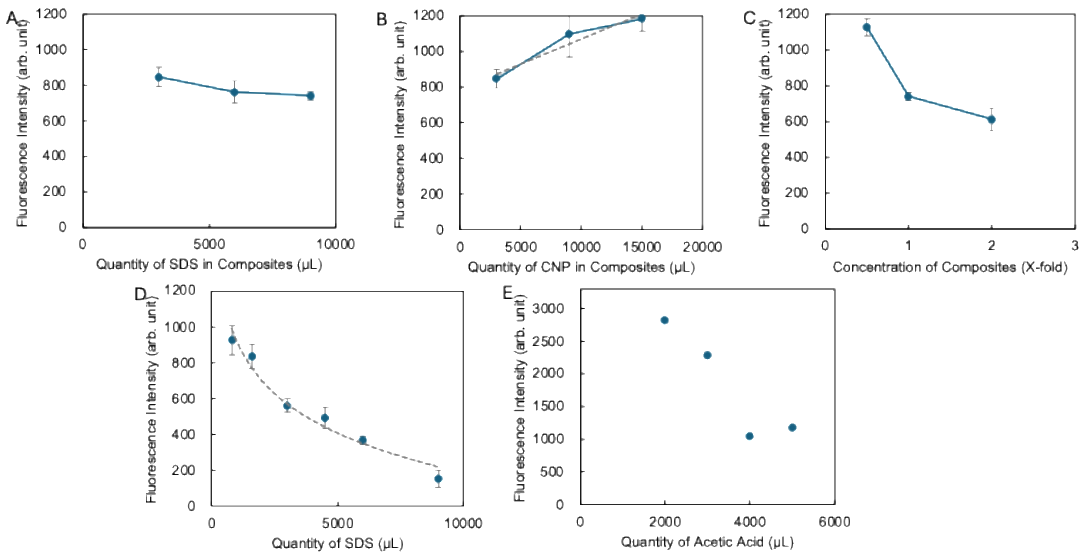

Fig. 16 Fluorescence intensity of TA solutions with composite samples (a, b, and c), SDS solutions(d) or acetic acid solutions(e).
(Ex: 315 nm, Em: 425nm. For graph a, b, c, and d: n = 3, mean ±S.D. *p < 0.05, Student's t-test).

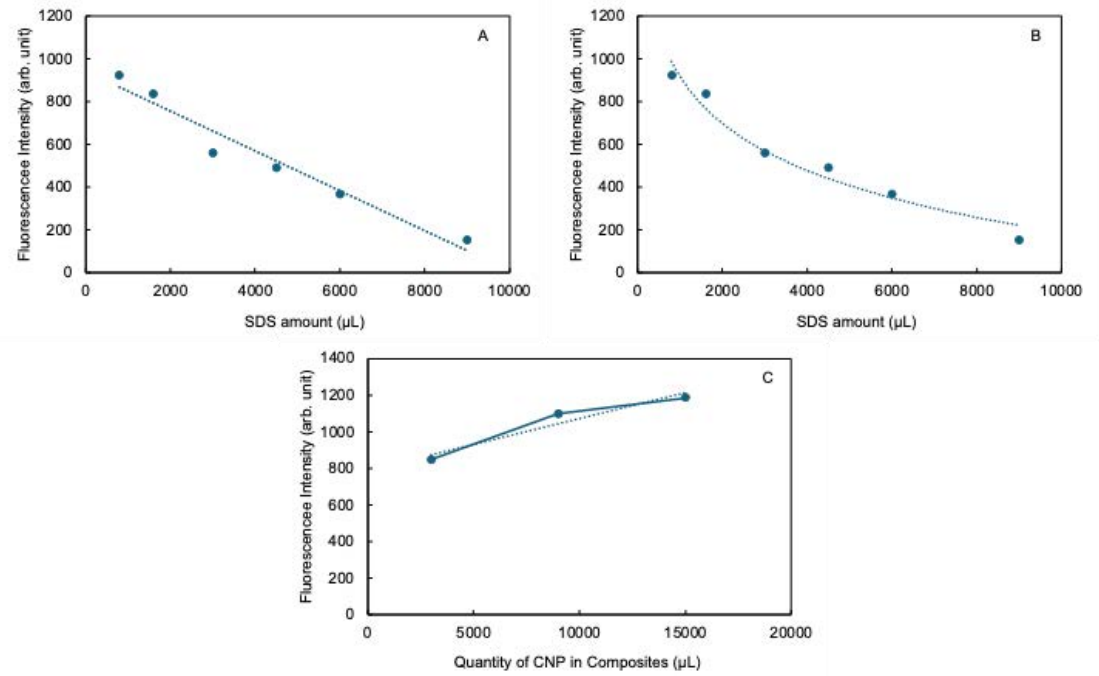

Fig. 17 Correlation between fluorescence intensity and SDS amount (figure a: linear fitting, figure b: logarithmic fitting), chitosan nanoparticle amount of composite (figure c: linear fitting). The x axis in figure c represents the quantity of chitosan nanoparticles in composites.

Table 2 Comparisons between experimental data and calculations based on the equations in figure 17 (a: R-squared; b: p from T test were also listed.). The experimental data points are from figure 16b & 16c.

(a)

Experimental Data	Linear Fitting(f=1)	Logarithmic Fitting(f=1)	Linear Fitting(f=0.7)	Logarithmic Fitting(f=0.7)	Linear Fitting(f=0.5)	Logarithmic Fitting(f=0.5)
8.47×10^{2}	7.47×10^{2}	6.54×10^{2}	8.31×10^{2}	7.67×10^{2}	8.86×10^{2}	8.73×10^{2}
7.61×10^{2}	4.68×10^{2}	4.34×10^{2}	6.36×10^{2}	5.47×10^{2}	7.47×10^{2}	6.54×10^{2}
7.41×10^{2}	1.90×10^{2}	3.05×10^{2}	4.40×10^{2}	4.18×10^{2}	6.08×10^{2}	5.25×10^{2}
1.13×10^{3}	5.66×10^{2}	4.83×10^{2}	6.91×10^{2}	5.96×10^{2}	7.75×10^{2}	7.03×10^{2}
7.41×10^{2}	1.90×10^{2}	3.05×10^{2}	4.40×10^{2}	4.18×10^{2}	6.08×10^{2}	5.25×10^{2}
6.12×10^{2}	-5.62×10^{2}	1.70×10^{2}	-6.05×10^{1}	2.83×10^{2}	2.74×10^{2}	3.90×10^{2}
R-squared	0.886	0.963	0.886	0.963	0.886	0.963
R-squared	0.795	0.960	0.795	0.960	0.795	0.960

(b) standardized

Experimental Data	Linear Fitting(f=1)	Logarithmic Fitting(f=1)	Linear Fitting(f=0.7)	Logarithmic Fitting(f=0.7)	Linear Fitting(f=0.5)	Logarithmic Fitting(f=0.5)
8.47×10^{2}	1.04×10^{3}	9.81×10^{2}	9.56×10^{2}	9.81×10^{2}	9.01×10^{2}	9.81×10^{2}
7.61×10^{2}	7.61×10^{2}	7.61×10^{2}	7.61×10^{2}	7.61×10^{2}	7.61×10^{2}	7.61×10^{2}
7.41×10^{2}	4.82×10^{2}	6.33×10^{2}	5.66×10^{2}	6.33×10^{2}	6.22×10^{2}	6.33×10^{2}
1.13×10^{3}	1.12×10^{3}	9.19×10^{2}	9.92×10^{2}	9.19×10^{2}	9.08×10^{2}	9.19×10^{2}
7.41×10^{2}	7.41×10^{2}	7.41×10^{2}	7.41×10^{2}	7.41×10^{2}	7.41×10^{2}	7.41×10^{2}
6.12×10^{2}	-1.06×10^{1}	6.06×10^{2}	2.40×10^{2}	6.06×10^{2}	4.07×10^{2}	6.06×10^{2}
T.test	0.906	0.942	0.867	0.942	0.820	0.942
T.test	0.607	0.716	0.569	0.716	0.545	0.716

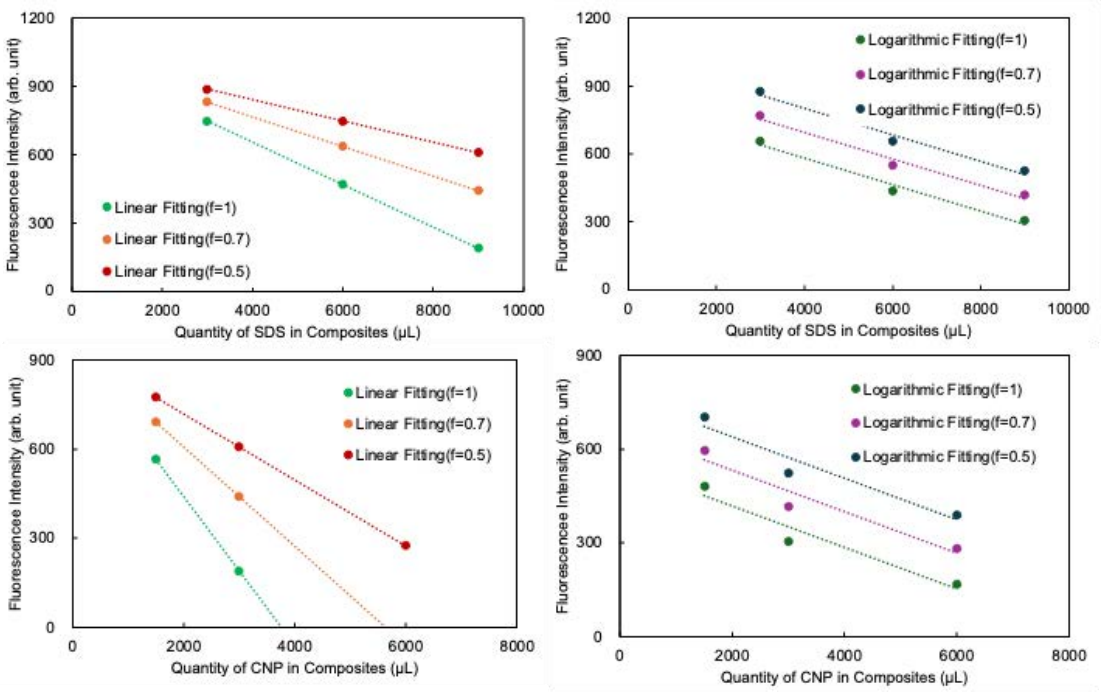

Fig. 18 Calculated fluorescence intensity values from Table 2a and their trendlines.

Generally, extended ultrasonic treatment time results in higher fluorescence intensity, as shown in Fig. 15. In the chitosan nanoparticles sample, the amount of CNP added was identical to that in sample “CNP3SDS2”, whereas the SDS added to the TA solution was adjusted to a ratio of 1.7 relative to CNP. The TA solution without any additives displayed the highest fluorescence intensity, suggesting that a more detailed analysis of the original data is needed to clarify the effect of each component. Sodium dodecyl sulfate can inhibit the fluorescence reaction of terephthalic acid by altering the microenvironment; the micelles formed by SDS may encapsulate TA molecules, thereby reducing their effective interaction with other reactive species. Furthermore, as an anionic surfactant, SDS carries a negative charge that can interfere with positively charged intermediates critical to the fluorescence process. Additionally, SDS may also competitively adsorb onto active sites, further restricting TA’s accessibility and lowering the overall fluorescence yield.

Figure 16 shows the fluorescence intensity peak values of ultrasound-treated TA solutions with the addition of CNP-shelled composites. The volume ratio between CNP

and SDS was varied. Figure 16a, 16b and 16c present the fluorescence intensity of TA solutions with composite samples. In Figure 16a, the volume of CNP was fixed at 3000 μL, while the amount of SDS was adjusted to alter the volume ratio during composite preparation. In Figure 16b, the volume of SDS solution was fixed at 3000 μL, while the quantity of CNP was varied. In Figure 16c, the composite sample had a volume ratio of 1:3 between CNP and SDS solution, using 3 mL of chitosan nanoparticles and 9 mL of SDS solution. The concentration of this composite sample was altered during the washing process before ultrasonic irradiation. Figure 16d shows the fluorescence intensity of TA solutions with SDS. A higher concentration of SDS solution (0.1 M) was used for the dilution of TA. The horizontal axis indicates the quantity calculated based on the standard SDS concentration (10 mM) used in synthesizing the composites. Figure 16e demonstrates that the presence of acetic acid influenced the fluorescence intensity. The intensity values were higher than those in other graphs, as both the ultrasound homogenizer output and the treatment time were altered to 30% and 30 minutes, respectively, for the experiments involving acetic acid. Acetic acid, used in the synthesis of chitosan nanoparticles, may have left some residual amounts, but the larger volume used here aimed to assess its potential effect on the fluorescence intensity results. The pure TA solution without composite samples showed a fluorescence intensity of 1.76×10^3, an average of 4 times the measurement.

Figure 16(a) shows a decreasing trend in fluorescence intensity with increasing SDS quantity, while Figure 16(b) demonstrates an increase in fluorescence intensity as the amount of CNP in the composites increases. In Figure 16(c), a decreasing trend in fluorescence intensity was observed with increasing the concentration of composite. These graphs collectively examine the effects of varying the concentrations and volume ratio of composites on fluorescence intensity. It is suggested that increasing the quantity of SDS, reducing the amount of chitosan nanoparticles in the composites, or increasing the composite concentration all lead to a reduction in the generation of hydroxyl

radicals, indicating a potential decrease in acoustic cavitation activity. As the concentration of chitosan nanoparticles increased, the amount of SDS also increased and was released under ultrasonic irradiation. Based on the results from Figures 16a, 16b, and 16c, the influence of the acoustic cavitation effect by different composite samples can be compared. The composite with the highest fluorescence intensity exhibited an increase of 93% compared to the composite with the lowest fluorescence intensity.

Figure 17 presents three graphs (a, b, and c) analyzing the impact of the amount of CNP or SDS solution on fluorescence intensity. Each graph includes fitted trendlines with corresponding equations and R-squared values. The data points were from Fig. 16b and 16d. Figure 17(a) reveals a strong negative correlation between fluorescence intensity and SDS amount, as evidenced by a linear fit: $y = (-9.29\times10^{-2})x + 9.41\times10^{-2}$ with $R^2 = 0.954$. Conversely, Fig. 17 (b) demonstrates a slightly better fit with a logarithmic trendline, $y = (-3.17\times10^{2})\ln(x) + 3.11\times10^{3}$ with $R^2 = 0.961$, suggesting a logarithmic decrease in fluorescence with increasing SDS. Finally, Fig. 17(c) displays a positive linear correlation between fluorescence and composite concentration, $y = (2.81\times10^{-2})x + 7.89\times10^{2}$ with $R^2 = 0.928$. In Figure 17(c), although the effect on SDS cannot be accurately estimated, it can be regarded as constant since the amount of SDS is constant. Thus, the equation of the nanoparticle is obtained: $y = (2.81\times10^{-2})x$.

The fluorescence intensity for a CNP-shelled composite synthesized with a μL of chitosan nanoparticles and b μL of SDS solution is expressed by a combination of the following functions

$$F(a,s) = CNP\,(a) + SDS\,(s) + c \tag{4-1}$$

$$CNP\,(a) = (2.81\times10^{-2})a \tag{4-2}$$

$$SDS(s) = (-9.29\times10^{-2})s + (9.41\times10^{2}) \tag{4-3-1}$$

$$SDS(s) = (-3.17\times10^{-2})\ln(s) + (3.11\times10^{3}) \tag{4-3-2}$$

$$s = f \times b \tag{4-3-3}$$

where a and b are the volume (μL) of chitosan nanoparticles and SDS solution, f is a fitting parameter that determines the contribution of residual SDS solution to the resultant fluorescence intensity, $F(a,s)$, and c is a constant. Here, we discuss which fitting models, noted by eq. (4-3-1) or eq. (4-3-2), are appropriate for formulating $F(a,s)$ and their applicable range of SDS concentration. The parameter f physically represents the fraction of the remaining volume of SDS after washing to the volume of SDS initially added in the composite synthesis. By choosing f as 0.5, 0.7, and 1.0, a series of $F(a,s)$ calculated using either linear or logarithmic models are compared to the measured fluorescence intensities labeled as "experimental data" in Table 2 for estimating the effect of the residual SDS on TA reaction. The experimental data from Figs. 16a and 16c involve various quantities of chitosan nanoparticles and SDS, which also means that the volume ratio was altered. The calculations were based on the previous equations (4-1 and 4-2) and the corresponding equations obtained from Fig. 17. The constant, c, is affected by the fluorescence intensity of pure TA solution and the residual SDS (Fig. 17c). The calculated values of composite are the sum of the equations for CNP and SDS because there is already a negative sign in the SDS(s) portion of the equation. Since the c in eq. (4-1) cannot be determined, the calculated values were standardized based on experimental data, by adding a constant to each value in Table 2a. The residual amount of SDS (in both the solution and the composite) after two washes was uncertain. Linear and logarithmic fitting models were evaluated with R-squared values and p-values from T-tests, indicating the reliability of each fitting method. From a physical perspective, the inhibitory effect of SDS on the TA reaction has an upper limit, making logarithmic fitting a more realistic model, especially at higher SDS amounts. Notably, logarithmic fittings consistently outperformed linear fittings in terms of R-squared values (highest R-squared = 0.963), suggesting a more accurate representation of the data. However, by comparing the first-row experimental data in the upper and lower sections of Table 2b (8.47×10^2 and 1.13×10^3), the values

calculated using linear fitting maintain the same trend as the experimental results. This indicates that linear fitting remains applicable at lower SDS concentrations. Additionally, these calculations can be used to estimate the fluorescence intensity of composite samples with known volume ratios, providing a basis for comparing their effects on acoustic cavitation.

Figure 18 contained four scatter plots with trendlines showing the calculated values using different fitting models and their trendlines. The calculated values were from Table 2a. Since the fitting parameter *f* represents the residual amount of SDS during TA reaction, Fig. 18 illustrates the influence of different SDS residual levels on the fluorescence intensity of composites with varying volume ratios.

The accuracy of the calculating models may be influenced by several factors. Firstly, the standard value of the TA solution must be measured for each set of experiments to ensure consistency. Secondly, the presence of residual acetic acid, introduced during the nanoparticle synthesis process, could affect the results (Fig. 16e). Additionally, maintaining consistent ultrasonic irradiation settings presents a challenge, potentially leading to variability in the fluorescence intensity data. Furthermore, experimental errors, which may necessitate repeated experiments, could introduce inconsistencies that impact the fitting model. Lastly, the structural differences among composite samples, influenced by their varying compositions, may also play a significant role in affecting the experimental data and the fitting models. These factors collectively contribute to the complexity and potential inaccuracies in the model fitting processes.

Since SDS is demonstrated to impede the TA reaction, the portion of the difference between the pure TA solution and SDS (*s*) may be identified as the part that is impacted by SDS and then be subtracted. Once the influence of SDS has been eliminated, its calculated values (obtained via logarithmic fitting in Fig. 17b) can be subtracted from

the composite experimental data (Fig. 16) to determine the composite's effect on TA (Fig. 19). The effect of CNP-shelled composites is expressed as follows:

$$Effect\ of\ CNP-shelled\ composites\ =\ Composite\ experimental\ data\ +\ (Fluorescence\ intensity\ of\ TA\ solution\ -\ Calculated\ values\ of\ SDS) \quad (4\text{-}4)$$

The intensity value of composite is higher than that of TA when $f \geq 0.418$. Composite has a recognized boosting influence on ultrasonic acoustic cavitation as known from KI dosimetry, and the trend of the calculated results agrees with the experimental data. Even if the parameter "f" has an impact on the absolute value, as the CNP in the composite grows, the promoting influence on TA continues to exhibit an upward trend.

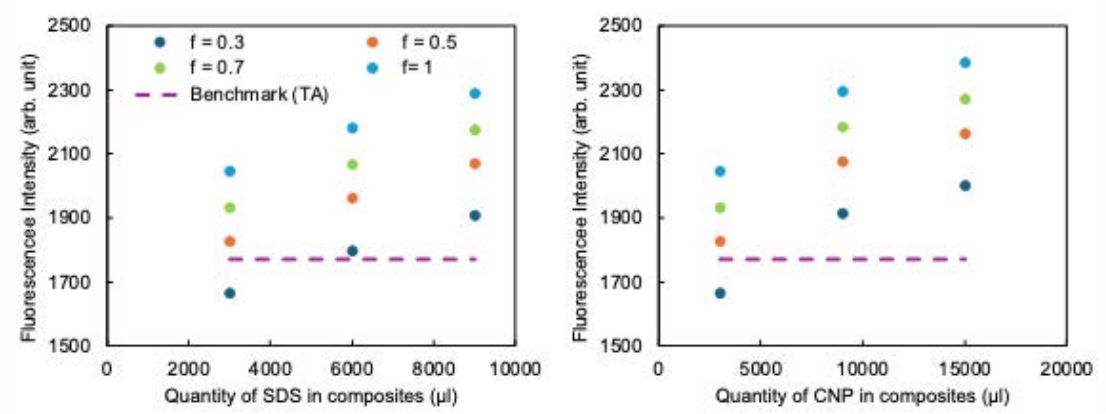

Fig. 19 Calculations showing the effect of chitosan nanoparticle-shelled composites, while subtracting the effect of SDS.

Composite has a recognized boosting influence on ultrasonic acoustic cavitation known from KI dosimetry, and the trend of the calculated results agrees with the experimental data.

4.4 Summary

In this chapter, the enhancement of acoustic cavitation using chitosan nanoparticle-shelled composites was analyzed. These composites were synthesized by varying shaking time, shaking speed, and the volume ratio between chitosan nanoparticles and SDS solution. The primary focus was on evaluating the effects of ultrasound on acoustic cavitation, with iodide dosimetry and terephthalic acid dosimetry serving as key measurement techniques. These methods provided both direct and indirect evidence of the composites' performance in enhancing cavitation.

Iodide dosimetry leverages the oxidation of potassium iodide to measure cavitation activity. In these experiments, various CNP-shelled nanocomposites were synthesized by adjusting the volume ratio between SDS and chitosan nanoparticles and altering shaking speeds. The absorbance of I_3^- ions, formed during KI oxidation under ultrasound, was measured using UV spectroscopy. Results indicated that composites synthesized at 1200 rpm showed better performance in enhancing ultrasound effects compared to those synthesized at 750 rpm, likely due to differences in composite sizes. Despite this, the specific impact of the ratio between chitosan nanoparticles and SDS on ultrasound enhancement remained unclear, as trends were not consistently observed. Nevertheless, samples with added chitosan nanoparticles or composites consistently showed higher peak absorbance values than those with only KI and SDS, confirming the enhancement of ultrasound by the composites.

To address limitations in iodide dosimetry, particularly the formation of chitosan-iodine complexes that could distort quantitative measurements, TA dosimetry was employed. This method measures free hydroxyl radicals produced during cavitation bubble collapse, providing a more precise analysis of cavitation activity. Despite challenges in dissolving TA in water and ensuring the stability of chitosan composites, TA dosimetry revealed significant insights. Fluorescence intensity peak values were measured for various TA solutions and composites, with results indicating that prolonged ultrasonic treatment generally led to higher fluorescence intensity. The analysis showed that increasing SDS quantity decreased fluorescence intensity, while increasing chitosan nanoparticles in the composites led to higher fluorescence intensity. These findings suggest a complex interplay between the components of the composites and their effects on cavitation enhancement.

In conclusion, this chapter demonstrated that CNP-shelled composites can enhance

acoustic cavitation, with variations in synthesis conditions influencing their effectiveness. While iodide dosimetry provided initial insights, TA dosimetry offered more precise quantitative analysis, despite its challenges. Future experiments should focus on optimizing composite synthesis and dosimetry methods to further clarify the mechanisms of ultrasound enhancement and improve the reliability of quantitative measurements.

Chapter 5 General Conclusions and Outlook

5.1 Conclusions

To enhance the effect of ultrasound, a structure with gas bubbles as the cores and chitosan nanoparticles as the shell has been proposed. This study has delved into the synthesis, characterization, and application of chitosan nanoparticle-shelled composites, focusing on their potential to enhance acoustic cavitation and lay the groundwork for various therapeutic and industrial applications. This composite is thought to be promising for drug delivery or initiating chemical reactions, mainly because of acoustic cavitation.

By adjusting the amount of crosslinker or its concentration, the size of chitosan nanoparticles can be controlled from approximately 20 nm to several hundred nanometers. The process of loading proteins into nanoparticles alters their size, with a loading efficiency exceeding 90%. The application of ultrasound and chitosan nanocarriers effectively increases the concentration of bFGF, with higher ultrasound intensities yielding better delivery outcomes. It has been demonstrated that carboxymethyl chitosan nanocarriers, when combined with ultrasound, successfully deliver bFGF into hairless mouse skin ex vivo. The enhancement observed in the presence of chitosan nanocarriers is attributed to the acoustic cavitation effect, though the specific influencing factors require further investigation. The ability of chitosan nanoparticles to load proteins has been well established, suggesting that even if the composites are disrupted by ultrasonic irradiation, the drug carriers can still fulfill their function. Sonophoresis, which employs ultrasound to disrupt the structure of the stratum corneum, facilitates the transdermal delivery of macromolecules and has demonstrated promising results for drugs such as heparin, insulin, and other peptides. Conventional studies have primarily focused on the size of drugs transdermally delivered by sonophoresis alone. However, contrary to previous findings, this study

suggests that increasing the size of nanocarriers can enhance bFGF delivery efficiency when combined with sonophoresis. These results indicate that the protection provided by degradable nanomedicine, along with the effects of acoustic cavitation from additives, may influence sonophoresis performance. Therefore this study focused on designing chitosan nanoparticle-shelled composites, which hold the promise for various applications based on their ability to enhance acoustic cavitation.

By changing the size of chitosan nanoparticles, the shaking speed or time, and the volume ratio between CNPs and SDS, the size of the composites seems to be adjustable. To prepare CNP-shelled composites, longer shaking times and higher volume ratios between the CNP suspension and SDS solution are preferable. Extended shaking durations provide sufficient energy for the migration and deposition of CNPs at the gas-core interface, ensuring a stable and complete shell structure. The composite's ability to load drugs can be achieved by preparing composites with drug-contained nanoparticles.

Qualitative analysis by KI dosimetry has proven that the composites can enhance ultrasonic effects. The SDS benchmark showed a 1.12-fold improvement over ultrasonically treated sodium iodide solution decomposition. The use of composites enhanced hydroxyl radical generation by 1.73- to 1.98-fold, surpassing SDS by 54% to 77%, suggesting enhanced acoustic cavitation. Moreover, the study highlights the complex interplay between various experimental parameters and their impact on the fluorescence intensity of TA solutions. Increasing the quantity of SDS or reducing the amount of chitosan nanoparticles in the composites, as well as increasing the concentration of the composite, consistently led to a decrease in fluorescence intensity. Through rigorous analysis, linear and logarithmic fitting models were employed to understand these relationships, with logarithmic models demonstrating a higher accuracy as indicated by superior R-squared values. The investigation also underscored

the significance of considering residual SDS, acetic acid presence, and experimental consistency in influencing the results. Ultimately, recent results provided valuable insights into predicting fluorescence intensity through composite formulations. Composite has a recognized boosting influence on ultrasonic acoustic cavitation known from KI dosimetry, and the trend of the calculated results agrees with the experimental data from TA dosimetry. Even if the residual SDS remained unclear, as the CNP in the composite grows, the promoting influence on TA continues to exhibit an upward trend.

Despite promising results, several limitations need to be addressed. The synthesis process for chitosan microbubbles is not complex but requires optimization to ensure consistent and reproducible results. Additionally, factors such as bubble size, shell thickness, and ultrasound parameters significantly affect drug or gene delivery efficiency, requiring extensive in vitro and in vivo studies to optimize these variables.

5.2 Outlook

The potential of chitosan-shelled composites for enhancing acoustic cavitation is evident from the experimental data. Future experiments should focus on optimizing synthesis methods and dosimetry techniques to further elucidate the mechanisms of ultrasound enhancement and improve the reliability of quantitative measurements. Additionally, exploring the use of these composites in emerging fields such as regenerative medicine and environmental applications holds significant promise. The findings from this study contribute to the broader understanding of acoustic cavitation and its enhancement through nanocomposites, paving the way for innovative applications in medicine and industry. As research progresses, it is crucial to address the existing limitations while harnessing the full potential of chitosan-shelled composites for practical and impactful solutions.

Recent research has made strides in overcoming the limitations of microbubbles, focusing on enhancing the functionality of microbubbles. Innovations include developing multifunctional microbubbles that combine drug delivery with diagnostic imaging, offering a theranostic approach. Issues such as poor solubility of chitosan in neutral and basic conditions, limited drug loading capacity, and potential toxicity of modified chitosan derivatives need to be addressed [10–12,15,103]. Surface modifications with targeting ligands have been explored to improve specificity towards diseased tissues. Studies have also investigated the use of chitosan derivatives and co-polymers to enhance the stability and reduce the immunogenicity of the microbubbles [10,152].

References

[1] J. Seo, Y. sun Kim, Ultrasound imaging and beyond: recent advances in medical ultrasound, Biomed. Eng. Lett. 7 (2017) 57–58. https://doi.org/10.1007/s13534-017-0030-7.

[2] D.L. Miller, N.B. Smith, M.R. Bailey, G.J. Czarnota, K. Hynynen, I.R.S. Makin, Overview of therapeutic ultrasound applications and safety considerations, J. Ultrasound Med. 31 (2012) 623–634. https://doi.org/10.7863/jum.2012.31.4.623.

[3] C.M. Moran, A.J.W. Thomson, Preclinical Ultrasound Imaging—A Review of Techniques and Imaging Applications, Front. Phys. 8 (2020) 124. https://doi.org/10.3389/fphy.2020.00124.

[4] M.R. Bailey, V.A. Khokhlova, O.A. Sapozhnikov, S.G. Kargl, L.A. Crum, Physical mechanisms of the therapeutic effect of ultrasound (a review), Acoust. Phys. 49 (2003) 369–388. https://doi.org/10.1134/1.1591291.

[5] T. Leong, M. Ashokkumar, S. Kentish, THE FUNDAMENTALS OF POWER ULTRASOUND - A REVIEW, Acoust. Aust. 39 (2011) 54–63. https://www.semanticscholar.org/paper/THE-FUNDAMENTALS-OF-POWER-ULTRASOUND-A-REVIEW-Leong-Ashokkumar/4aa9280f1e7df7336d2545d5708fef6ec14868f7.

[6] Y. Yao, Y. Pan, S. Liu, Power ultrasound and its applications: A state-of-the-art review, Ultrason. Sonochem. 62 (2020) 104722. https://doi.org/10.1016/j.ultsonch.2019.104722.

[7] M.T. Gevari, T. Abbasiasl, S. Niazi, M. Ghorbani, A. Koşar, Direct and indirect thermal applications of hydrodynamic and acoustic cavitation: A review, Appl. Therm. Eng. 171 (2020) 115065. https://doi.org/10.1016/j.applthermaleng.2020.115065.

[8] D. Dalecki, Mechanical bioeffects of ultrasound, Annu. Rev. Biomed. Eng. 6 (2004) 229–248. https://doi.org/10.1146/annurev.bioeng.6.040803.140126.

[9] K.S. Suslick, Applications of Ultrasound to Materials Chemistry, MRS Bull. 20 (1995) 29–34. https://doi.org/10.1557/S088376940004464X.

[10] P. Agrawal, G.J. Strijkers, K. Nicolay, Chitosan-based systems for molecular imaging, Adv. Drug Deliv. Rev. 62 (2010) 42–58. https://doi.org/10.1016/j.addr.2009.09.007.

[11] X. Xiong, F. Zhao, M. Shi, H. Yang, Y. Liu, Polymeric Microbubbles for Ultrasonic Molecular Imaging and Targeted Therapeutics, J. Biomater. Sci. Polym. Ed. 22 (2011) 417–428. https://doi.org/10.1163/092050610X540440.

[12] L.M. Tay, C. Xu, Coating Microbubbles With Nanoparticles for Medical Imaging and Drug Delivery, Nanomedicine. 12 (2017) 91–94. https://doi.org/10.2217/nnm-2016-0362.

[13] J. Rodríguez-Rodríguez, A. Sevilla, C. Martínez-Bazán, J.M. Gordillo, Generation of microbubbles with applications to industry and medicine, Annu. Rev. Fluid Mech. 47 (2015) 405–429. https://doi.org/10.1146/annurev-fluid-010814-014658.

[14] C. Zhang, Y. Li, X. Ma, W. He, C. Liu, Z. Liu, Functional micro/nanobubbles for ultrasound medicine and visualizable guidance, Sci. China Chem. 64 (2021) 899–914. https://doi.org/10.1007/s11426-020-9945-4.

[15] R. Xiong, R.X. Xu, C. Huang, S. De Smedt, K. Braeckmans, Stimuli-responsive nanobubbles for biomedical applications, Chem. Soc. Rev. 50 (2021) 5746–5776.

https://doi.org/10.1039/C9CS00839J.

[16] A. Jamburidze, A. Huerre, D. Baresch, V. Poulichet, M. De Corato, V. Garbin, Nanoparticle-Coated Microbubbles for Combined Ultrasound Imaging and Drug Delivery, Langmuir. 35 (2019) 10087–10096. https://doi.org/10.1021/acs.langmuir.8b04008.

[17] H. Lee, H. Kim, H. Han, M. Lee, S. Lee, H. Yoo, J.H. Chang, H. Kim, Microbubbles used for contrast enhanced ultrasound and theragnosis: a review of principles to applications, Biomed. Eng. Lett. 7 (2017) 59–69. https://doi.org/10.1007/s13534-017-0016-5.

[18] Q. Huang, Z. Zeng, A Review on Real-Time 3D Ultrasound Imaging Technology, Biomed Res. Int. 2017 (2017). https://doi.org/10.1155/2017/6027029.

[19] F.S. Foster, C.J. Pavlin, K.A. Harasiewicz, D.A. Christopher, D.H. Turnbull, Advances in ultrasound biomicroscopy, Ultrasound Med. Biol. 26 (2000) 1–27. https://doi.org/10.1016/S0301-5629(99)00096-4.

[20] J. Du, X.-L. Mao, P.-F. Ye, Q.-H. Huang, Three-Dimensional Reconstruction and Visualization of Human Enamel Ex Vivo Using High-Frequency Ultrasound, J. Med. Biol. Eng. 37 (2017) 112–122. https://doi.org/10.1007/s40846-016-0213-1.

[21] P.R. Hoskins, Principles of ultrasound elastography, Ultrasound. 20 (2012) 8–15. https://doi.org/10.1258/ult.2011.011005.

[22] J. Bamber, D. Cosgrove, C. Dietrich, J. Fromageau, J. Bojunga, F. Calliada, V. Cantisani, J.-M. Correas, M. D'Onofrio, E. Drakonaki, M. Fink, M. Friedrich-Rust, O. Gilja, R. Havre, C. Jenssen, A. Klauser, R. Ohlinger, A. Saftoiu, F. Schaefer, I. Sporea, F. Piscaglia, EFSUMB Guidelines and Recommendations on the Clinical Use of Ultrasound Elastography. Part 1: Basic Principles and Technology, Ultraschall Der Medizin - Eur. J. Ultrasound. 34 (2013) 169–184. https://doi.org/10.1055/s-0033-1335205.

[23] H. Yoon, S.K. Yarmoska, A.S. Hannah, C. Yoon, K.A. Hallam, S.Y. Emelianov, Contrast-enhanced ultrasound imaging in vivo with laser-activated nanodroplets, Med. Phys. 44 (2017) 3444–3449. https://doi.org/10.1002/mp.12269.

[24] W.K. Chong, V. Papadopoulou, P.A. Dayton, Imaging with ultrasound contrast agents: current status and future, Abdom. Radiol. 43 (2018) 762–772. https://doi.org/10.1007/s00261-018-1516-1.

[25] M. Versluis, E. Stride, G. Lajoinie, B. Dollet, T. Segers, Ultrasound Contrast Agent Modeling: A Review, Ultrasound Med. Biol. 46 (2020) 2117–2144. https://doi.org/10.1016/j.ultrasmedbio.2020.04.014.

[26] G. ter Haar, Therapeutic applications of ultrasound, Prog. Biophys. Mol. Biol. 93 (2007) 111–129. https://doi.org/10.1016/j.pbiomolbio.2006.07.005.

[27] L.D. Alexander, D.R.D. Gilman, D.R. Brown, J.L. Brown, P.E. Houghton, Exposure to Low Amounts of Ultrasound Energy Does Not Improve Soft Tissue Shoulder Pathology: A Systematic Review, Phys. Ther. 90 (2010) 14–25. https://doi.org/10.2522/ptj.20080272.

[28] S.A. Sapareto, W.C. Dewey, Thermal dose determination in cancer therapy, Int. J. Radiat. Oncol. 10 (1984) 787–800. https://doi.org/10.1016/0360-3016(84)90379-1.

[29] C.M.C. Tempany, E.A. Stewart, N. McDannold, B.J. Quade, F.A. Jolesz, K. Hynynen, MR Imaging–guided Focused Ultrasound Surgery of Uterine Leiomyomas: A Feasibility Study, Radiology. 226 (2003) 897–905. https://doi.org/10.1148/radiol.2271020395.

[30] S. Thüroff, C. Chaussy, G. Vallancien, W. Wieland, H.J. Kiel, A. le Duc, F. Desgrandchamps, J.J.M.C.H. de la Rosette, A. Gelet, High-Intensity Focused Ultrasound and Localized Prostate Cancer: Efficacy Results from the European Multicentric Study, J. Endourol. 17 (2003) 673–677. https://doi.org/10.1089/089277903322518699.

[31] L.G. Merckel, F.M. Knuttel, R. Deckers, T. van Dalen, G. Schubert, N.H.G.M. Peters, T. Weits, P.J. van Diest, W.P.T.M. Mali, P.H.H.B. Vaessen, J.M.H.H. van Gorp, C.T.W. Moonen, L.W. Bartels, M.A.A.J. van den Bosch, First clinical experience with a dedicated MRI-guided high-intensity focused ultrasound system for breast cancer ablation, Eur. Radiol. 26 (2016) 4037–4046. https://doi.org/10.1007/s00330-016-4222-9.

[32] H.E. Elmansy, J.E. Lingeman, Recent advances in lithotripsy technology and treatment strategies: A systematic review update, Int. J. Surg. 36 (2016) 676–680. https://doi.org/10.1016/j.ijsu.2016.11.097.

[33] S. Rutten, M.P.J. van den Bekerom, I.N. Sierevelt, P.A. Nolte, Enhancement of Bone-Healing by Low-Intensity Pulsed Ultrasound, JBJS Rev. 4 (2016). https://doi.org/10.2106/JBJS.RVW.O.00027.

[34] A. Harrison, V. Alt, Low-intensity pulsed ultrasound (LIPUS) for stimulation of bone healing – A narrative review, Injury. 52 (2021) S91–S96. https://doi.org/10.1016/j.injury.2021.05.002.

[35] Z. Zhao, Q. Saiding, Z. Cai, M. Cai, W. Cui, Ultrasound technology and biomaterials for precise drug therapy, Mater. Today. 63 (2023) 210–238. https://doi.org/10.1016/j.mattod.2022.12.004.

[36] P. Wei, E.J. Cornel, J. Du, Ultrasound-responsive polymer-based drug delivery systems, Drug Deliv. Transl. Res. 11 (2021) 1323–1339. https://doi.org/10.1007/s13346-021-00963-0.

[37] J. Deprez, G. Lajoinie, Y. Engelen, S.C. De Smedt, I. Lentacker, Opening doors with ultrasound and microbubbles: Beating biological barriers to promote drug delivery, Adv. Drug Deliv. Rev. 172 (2021) 9–36. https://doi.org/10.1016/j.addr.2021.02.015.

[38] J. Rich, Z. Tian, T.J. Huang, Sonoporation: Past, Present, and Future, Adv. Mater. Technol. 7 (2022) 1–17. https://doi.org/10.1002/admt.202100885.

[39] J. Tu, A.C.H.H. Yu, Ultrasound-Mediated Drug Delivery: Sonoporation Mechanisms, Biophysics, and Critical Factors, BME Front. 2022 (2022) 40–43. https://doi.org/10.34133/2022/9807347.

[40] Y. Yang, Q. Li, X. Guo, J. Tu, D. Zhang, Mechanisms underlying sonoporation: Interaction between microbubbles and cells, Ultrason. Sonochem. 67 (2020) 105096. https://doi.org/10.1016/j.ultsonch.2020.105096.

[41] Y. Meng, K. Hynynen, N. Lipsman, Applications of focused ultrasound in the brain: from thermoablation to drug delivery, Nat. Rev. Neurol. 17 (2021) 7–22. https://doi.org/10.1038/s41582-020-00418-z.

[42] T. Wu, C. Huang, Y. Yao, Z. Du, Z. Liu, Suicide Gene Delivery System Mediated by Ultrasound-Targeted Microbubble Destruction: A Promising Strategy for Cancer Therapy, Hum. Gene Ther. 33 (2022) 1246–1259. https://doi.org/10.1089/hum.2022.152.

[43] A.P.G. Walsh, H.N. Gordon, K. Peter, X. Wang, Ultrasonic particles: An approach for

targeted gene delivery, Adv. Drug Deliv. Rev. 179 (2021) 113998. https://doi.org/10.1016/j.addr.2021.113998.

[44] N. Sayed, P. Allawadhi, A. Khurana, V. Singh, U. Navik, S.K. Pasumarthi, I. Khurana, A.K. Banothu, R. Weiskirchen, K.K. Bharani, Gene therapy: Comprehensive overview and therapeutic applications, Life Sci. 294 (2022) 120375. https://doi.org/10.1016/j.lfs.2022.120375.

[45] H. Zeng, H. Li, H. Shao, One-pot three-component Mannich-type reactions using Sulfamic acid catalyst under ultrasound irradiation, Ultrason. Sonochem. 16 (2009) 758–762. https://doi.org/10.1016/j.ultsonch.2009.03.008.

[46] D. Bandyopadhyay, S. Mukherjee, L.C. Turrubiartes, B.K. Banik, Ultrasound-assisted aza-Michael reaction in water: A green procedure, Ultrason. Sonochem. 19 (2012) 969–973. https://doi.org/10.1016/j.ultsonch.2011.11.009.

[47] M.C. Diwathe, P.R. Gogate, Ultrasound assisted intensified synthesis of 1-benzyloxy-4-nitrobenzene in the presence of phase transfer catalyst, Chem. Eng. J. 346 (2018) 438–446. https://doi.org/10.1016/j.cej.2018.04.027.

[48] Y.-N. Liu, D. Jin, X.-P. Lu, P.-F. Han, Study on degradation of dimethoate solution in ultrasonic airlift loop reactor, Ultrason. Sonochem. 15 (2008) 755–760. https://doi.org/10.1016/j.ultsonch.2007.12.004.

[49] B. Savun-Hekimoğlu, N.H. Ince, Decomposition of PPCPs by ultrasound-assisted advanced Fenton reaction: A case study with salicylic acid, Ultrason. Sonochem. 39 (2017) 243–249. https://doi.org/10.1016/j.ultsonch.2017.04.013.

[50] B. Savun-Hekimoğlu, N.H. Ince, Sonochemical and sonocatalytic destruction of methylparaben using raw, modified and SDS-intercalated particles of a natural clay mineral, Ultrason. Sonochem. 54 (2019) 233–240. https://doi.org/10.1016/j.ultsonch.2019.01.034.

[51] T. Benabdallah El-Hadj, J. Dosta, R. Márquez-Serrano, J. Mata-Álvarez, Effect of ultrasound pretreatment in mesophilic and thermophilic anaerobic digestion with emphasis on naphthalene and pyrene removal, Water Res. 41 (2007) 87–94. https://doi.org/10.1016/j.watres.2006.08.002.

[52] S.I. Pérez-Elvira, L.C. Ferreira, A. Donoso-Bravo, M. Fdz-Polanco, F. Fdz-Polanco, Full-stream and part-stream ultrasound treatment effect on sludge anaerobic digestion, Water Sci. Technol. 61 (2010) 1363–1372. https://doi.org/10.2166/wst.2010.893.

[53] V. Naddeo, V. Belgiorno, D. Kassinos, D. Mantzavinos, S. Meric, Ultrasonic degradation, mineralization and detoxification of diclofenac in water: Optimization of operating parameters, Ultrason. Sonochem. 17 (2010) 179–185. https://doi.org/10.1016/j.ultsonch.2009.04.003.

[54] A.H. Mahvi, M. Ghanbarian, S. Nasseri, A. Khairi, Mineralization and discoloration of textile wastewater by TiO2 nanoparticles, Desalination. 239 (2009) 309–316. https://doi.org/10.1016/j.desal.2008.04.002.

[55] B. Savun-Hekimoğlu, A Review on Sonochemistry and Its Environmental Applications, Acoustics. 2 (2020) 766–775. https://doi.org/10.3390/acoustics2040042.

[56] P.R. Gogate, Application of cavitational reactors for water disinfection: Current status and path forward, J. Environ. Manage. 85 (2007) 801–815.

https://doi.org/10.1016/j.jenvman.2007.07.001.

[57] Z. Wang, C. Yin, State-of-the-art on ultrasonic oil production technique for EOR in China, Ultrason. Sonochem. 38 (2017) 553–559. https://doi.org/10.1016/j.ultsonch.2017.03.035.

[58] X. Huang, C. Zhou, Q. Suo, L. Zhang, S. Wang, Experimental study on viscosity reduction for residual oil by ultrasonic, Ultrason. Sonochem. 41 (2018) 661–669. https://doi.org/10.1016/j.ultsonch.2017.09.021.

[59] Z. Wang, Y. Xu, Y. Gu, Lithium niobate ultrasonic transducer design for Enhanced Oil Recovery, Ultrason. Sonochem. 27 (2015) 171–177. https://doi.org/10.1016/j.ultsonch.2015.05.017.

[60] Z. Wang, Y. Xu, The development of recent high-power ultrasonic transducers for Near-well ultrasonic processing technology, Ultrason. Sonochem. 37 (2017) 536–541. https://doi.org/10.1016/j.ultsonch.2017.01.043.

[61] J.B. Fowlkes, Bioeffects Committee of the American Institute of Ultrasound in Medicine, American Institute of Ultrasound in Medicine Consensus Report on Potential Bioeffects of Diagnostic Ultrasound, J. Ultrasound Med. 27 (2008) 503–515. https://doi.org/10.7863/jum.2008.27.4.503.

[62] J. Silberstein, C.M. Lakin, J. Kellogg Parsons, Shock wave lithotripsy and renal hemorrhage., Rev. Urol. 10 (2008) 236–41. http://www.ncbi.nlm.nih.gov/pubmed/18836562.

[63] W. Hundt, E.L. Yuh, M.D. Bednarski, S. Guccione, Gene Expression Profiles, Histologic Analysis, and Imaging of Squamous Cell Carcinoma Model Treated with Focused Ultrasound Beams, Am. J. Roentgenol. 189 (2007) 726–736. https://doi.org/10.2214/AJR.07.2371.

[64] E.M. Alves, A.T. Angrisani, M.B. Santiago, The use of extracorporeal shock waves in the treatment of osteonecrosis of the femoral head: a systematic review, Clin. Rheumatol. 28 (2009) 1247–1251. https://doi.org/10.1007/s10067-009-1231-y.

[65] T.J. Mason, Sonochemistry and the environment – Providing a “green” link between chemistry, physics and engineering, Ultrason. Sonochem. 14 (2007) 476–483. https://doi.org/10.1016/j.ultsonch.2006.10.008.

[66] R. Singla, M. Ashokkumar, F. Grieser, The mechanism of the sonochemical degradation of benzoic acid in aqueous solutions, Res. Chem. Intermed. 30 (2004) 723–733. https://doi.org/10.1163/1568567041856963.

[67] J.J. Hinman, K.S. Suslick, Nanostructured Materials Synthesis Using Ultrasound, in: 2017: pp. 59–94. https://doi.org/10.1007/978-3-319-54271-3_3.

[68] E.F. Karamah, R. Ghaudenson, F. Amalia, S. Bismo, Disinfection of Escherichia coli bacteria using hybrid method of ozonation and hydrodynamic cavitation with orifice plate, in: 2017: p. 020075. https://doi.org/10.1063/1.5011932.

[69] P. Zhong, Y. Zhou, Suppression of large intraluminal bubble expansion in shock wave lithotripsy without compromising stone comminution: Methodology and in vitro experiments, J. Acoust. Soc. Am. 110 (2001) 3283–3291. https://doi.org/10.1121/1.1416906.

[70] A.P. Evan, L.R. Willis, J.A. McAteer, M.R. Bailey, B.A. Connors, Y. Shao, J.E. Lingeman, J.C. Williams, N.S. Fineberg, L.A. Crum, Kidney Damage and Renal Functional Changes are Minimized by Waveform Control that Suppresses Cavitation in Shock Wave Lithotripsy,

J. Urol. 168 (2002) 1556–1562. https://doi.org/10.1016/S0022-5347(05)64520-X.

[71] H. Kiani, D.-W. Sun, Z. Zhang, The effect of ultrasound irradiation on the convective heat transfer rate during immersion cooling of a stationary sphere, Ultrason. Sonochem. 19 (2012) 1238–1245. https://doi.org/10.1016/j.ultsonch.2012.04.009.

[72] N.E. Hotrum, P. de Jong, J.C. Akkerman, M.B. Fox, Pilot scale ultrasound enabled plate heat exchanger – Its design and potential to prevent biofouling, J. Food Eng. 153 (2015) 81–88. https://doi.org/10.1016/j.jfoodeng.2014.11.026.

[73] T. Hou, Y. Chen, Z. Wang, C. Ma, Experimental study of fouling process and antifouling effect in convective heat transfer under ultrasonic treatment, Appl. Therm. Eng. 140 (2018) 671–678. https://doi.org/10.1016/j.applthermaleng.2018.04.021.

[74] F.-C. Liu, S.-W. Chen, J.-D. Lee, Feasibility Study of Heat Transfer Enhancement by Ultrasonic Vibration Under Subcooled Pool Condition, Heat Transf. Eng. 39 (2018) 654–662. https://doi.org/10.1080/01457632.2017.1325672.

[75] O. Bulliard-Sauret, J. Berindei, S. Ferrouillat, L. Vignal, A. Memponteil, C. Poncet, J.M. Leveque, N. Gondrexon, Heat transfer intensification by low or high frequency ultrasound: Thermal and hydrodynamic phenomenological analysis, Exp. Therm. Fluid Sci. 104 (2019) 258–271. https://doi.org/10.1016/j.expthermflusci.2019.03.003.

[76] E. Souza da Silva, S.C. Rupert Brandão, A. Lopes da Silva, J.H. Fernandes da Silva, A.C. Duarte Coêlho, P.M. Azoubel, Ultrasound-assisted vacuum drying of nectarine, J. Food Eng. 246 (2019) 119–124. https://doi.org/10.1016/j.jfoodeng.2018.11.013.

[77] J. Szadzińska, S.J. Kowalski, M. Stasiak, Microwave and ultrasound enhancement of convective drying of strawberries: Experimental and modeling efficiency, Int. J. Heat Mass Transf. 103 (2016) 1065–1074. https://doi.org/10.1016/j.ijheatmasstransfer.2016.08.001.

[78] R.D.A. Amaral, I. Achaerandio, B.C. Benedetti, M. Pujolà, The influence of edible coatings, blanching and ultrasound treatments on quality attributes and shelf-life of vacuum packaged potato strips, LWT - Food Sci. Technol. 85 (2017) 449–455. https://doi.org/10.1016/j.lwt.2017.03.062.

[79] A. Nikseresht, A. Daniyali, M. Ali-Mohammadi, A. Afzalinia, A. Mirzaie, Ultrasound-assisted biodiesel production by a novel composite of Fe(III)-based MOF and phosphotangestic acid as efficient and reusable catalyst, Ultrason. Sonochem. 37 (2017) 203–207. https://doi.org/10.1016/j.ultsonch.2017.01.011.

[80] A. Mosyak, G. Hetsroni, M. Fichman, L. Moldavsky, E. Pogrebnyak, Effect of heater size on ultrasonic enhancement of boiling in water and surfactant solutions, Int. J. Multiph. Flow. 79 (2016) 181–189. https://doi.org/10.1016/j.ijmultiphaseflow.2015.11.005.

[81] S.J. Kowalski, A. Pawłowski, Intensification of apple drying due to ultrasound enhancement, J. Food Eng. 156 (2015) 1–9. https://doi.org/10.1016/j.jfoodeng.2015.01.023.

[82] Y. Chen, S. Sun, Y. Lai, C. Ma, Influence of ultrasound to convectional heat transfer with fouling of cooling water, Appl. Therm. Eng. 100 (2016) 340–347. https://doi.org/10.1016/j.applthermaleng.2016.01.144.

[83] S. Both, F. Chemat, J. Strube, Extraction of polyphenols from black tea – Conventional and ultrasound assisted extraction, Ultrason. Sonochem. 21 (2014) 1030–1034. https://doi.org/10.1016/j.ultsonch.2013.11.005.

[84] S.V. Pereira, F.B. Colombo, L.A.P. de Freitas, Ultrasound influence on the solubility of solid dispersions prepared for a poorly soluble drug, Ultrason. Sonochem. 29 (2016) 461–469. https://doi.org/10.1016/j.ultsonch.2015.10.022.

[85] A. Schroeder, Y. Avnir, S. Weisman, Y. Najajreh, A. Gabizon, Y. Talmon, J. Kost, Y. Barenholz, Controlling Liposomal Drug Release with Low Frequency Ultrasound: Mechanism and Feasibility, Langmuir. 23 (2007) 4019–4025. https://doi.org/10.1021/la0631668.

[86] W.T. Yuen, S.C. Fu, J.K.C. Kwan, C.Y.H. Chao, The Use of Nonlinear Acoustics as an Energy-Efficient Technique for Aerosol Removal, Aerosol Sci. Technol. 48 (2014) 907–915. https://doi.org/10.1080/02786826.2014.938800.

[87] Y.B. Zhong, C.S. Wu, G.K. Padhy, Effect of ultrasonic vibration on welding load, temperature and material flow in friction stir welding, J. Mater. Process. Technol. 239 (2017) 273–283. https://doi.org/10.1016/j.jmatprotec.2016.08.025.

[88] Y. CUI, C. XU, Q. HAN, Effect of ultrasonic vibration on unmixed zone formation, Scr. Mater. 55 (2006) 975–978. https://doi.org/10.1016/j.scriptamat.2006.08.035.

[89] H.W. Kim, S.H. Cho, Y.Y. Kim, Analysis of internal wave reflection within a magnetostrictive patch transducer for high-frequency guided torsional waves, Ultrasonics. 51 (2011) 647–652. https://doi.org/10.1016/j.ultras.2011.02.004.

[90] Ben Amar Cheba, Chitin and Chitosan: Marine Biopolymers with Unique Properties and Versatile Applications, 6 (2011) 149–153. http://idosi.org/gjbb/gjbb6%283%2911/7.pdf.

[91] K.A. Janes, P. Calvo, M.J. Alonso, Polysaccharide colloidal particles as delivery systems for macromolecules, Adv. Drug Deliv. Rev. 47 (2001) 83–97. https://doi.org/10.1016/S0169-409X(00)00123-X.

[92] P. Calvo, C. Remuñán-López, J.L. Vila-Jato, M.J. Alonso, Novel hydrophilic chitosan-polyethylene oxide nanoparticles as protein carriers, J. Appl. Polym. Sci. 63 (1997) 125–132. https://doi.org/10.1002/(SICI)1097-4628(19970103)63:1<125::AID-APP13>3.0.CO;2-4.

[93] H. Fang, J. Huang, L. Ding, M. Li, Z. Chen, Preparation of magnetic chitosan nanoparticles and immobilization of laccase, J. Wuhan Univ. Technol. Sci. Ed. 24 (2009) 42–47. https://doi.org/10.1007/s11595-009-1042-7.

[94] F. Atyabi, F. Talaie, R. Dinarvand, Thiolated Chitosan Nanoparticles as an Oral Delivery System for Amikacin: In Vitro and Ex Vivo Evaluations, J. Nanosci. Nanotechnol. 9 (2009) 4593–4603. https://doi.org/10.1166/jnn.2009.1090.

[95] C. Chauvierre, D. Labarre, P. Couvreur, C. Vauthier, Radical Emulsion Polymerization of Alkylcyanoacrylates Initiated by the Redox System Dextran−Cerium(IV) under Acidic Aqueous Conditions, Macromolecules. 36 (2003) 6018–6027. https://doi.org/10.1021/ma034097w.

[96] S. Sajeesh, C.P. Sharma, Novel pH responsive polymethacrylic acid–chitosan–polyethylene glycol nanoparticles for oral peptide delivery, J. Biomed. Mater. Res. Part B Appl. Biomater. 76B (2006) 298–305. https://doi.org/10.1002/jbm.b.30372.

[97] I. Bravo-Osuna, C. Vauthier, A. Farabollini, G.F. Palmieri, G. Ponchel, Mucoadhesion mechanism of chitosan and thiolated chitosan-poly(isobutyl cyanoacrylate) core-shell

nanoparticles, Biomaterials. 28 (2007) 2233–2243. https://doi.org/10.1016/j.biomaterials.2007.01.005.

[98] K. Chandra Hembram, S. Prabha, R. Chandra, B. Ahmed, S. Nimesh, Advances in preparation and characterization of chitosan nanoparticles for therapeutics, Artif. Cells, Nanomedicine, Biotechnol. 44 (2016) 305–314. https://doi.org/10.3109/21691401.2014.948548.

[99] B. Sarmento, A.J. Ribeiro, F. Veiga, D.C. Ferreira, R.J. Neufeld, Insulin-Loaded Nanoparticles are Prepared by Alginate Ionotropic Pre-Gelation Followed by Chitosan Polyelectrolyte Complexation, J. Nanosci. Nanotechnol. 7 (2007) 2833–2841. https://doi.org/10.1166/jnn.2007.609.

[100] J.-H. Kim, Y.-S. Kim, K. Park, S. Lee, H.Y. Nam, K.H. Min, H.G. Jo, J.H. Park, K. Choi, S.Y. Jeong, R.-W. Park, I.-S. Kim, K. Kim, I.C. Kwon, Antitumor efficacy of cisplatin-loaded glycol chitosan nanoparticles in tumor-bearing mice, J. Control. Release. 127 (2008) 41–49. https://doi.org/10.1016/j.jconrel.2007.12.014.

[101] H.-Y. Huang, Y.-T. Shieh, C.-M. Shih, Y.-K. Twu, Magnetic chitosan/iron (II, III) oxide nanoparticles prepared by spray-drying, Carbohydr. Polym. 81 (2010) 906–910. https://doi.org/10.1016/j.carbpol.2010.04.003.

[102] J.J. Wang, Z.W. Zeng, R.Z. Xiao, T. Xie, G.L. Zhou, X.R. Zhan, S.L. Wang, Recent advances of chitosan nanoparticles as drug carriers., Int. J. Nanomedicine. 6 (2011) 765–774. https://doi.org/10.2147/ijn.s17296.

[103] Jhanvi Jhaveri, Zarna Raichura, Tabassum Khan, Munira Momin, AbdelWahab Omri, J. Jhaveri, Z. Raichura, T. Khan, M. Momin, A. Omri, Chitosan Nanoparticles-Insight into Properties, Functionalizationand Applications in Drug Delivery and Theranostics, Molecules. 26 (2021) 272. https://doi.org/10.3390/molecules26020272.

[104] Y. Wang, J. Qian, M. Yang, W. Xu, J. Wang, G. Hou, L. Ji, A. Suo, Doxorubicin/cisplatin co-loaded hyaluronic acid/chitosan-based nanoparticles for in vitro synergistic combination chemotherapy of breast cancer, Carbohydr. Polym. 225 (2019) 115206. https://doi.org/10.1016/j.carbpol.2019.115206.

[105] B.Y. Al-najjar, S.A. Hussain, CHITOSAN MICROSPHERES FOR THE DELIVERY OF CHEMOTHERAPEUTIC AGENTS: PACLITAXEL AS A MODEL, Asian J. Pharm. Clin. Res. 10 (2017) 15. https://doi.org/10.22159/ajpcr.2017.v10i8.18765.

[106] V. Sava, O. Fihurka, A. Khvorova, J. Sanchez-Ramos, Data on enrichment of chitosan nanoparticles for intranasal delivery of oligonucleotides to the brain, Data Br. 28 (2020) 105093. https://doi.org/10.1016/j.dib.2019.105093.

[107] R. Nasri, M. Hamdi, S. Touir, S. Li, M. Karra-Chaâbouni, M. Nasri, Development of delivery system based on marine chitosan: Encapsulationand release kinetic study of antioxidant peptides from chitosan microparticle, Int. J. Biol. Macromol. 167 (2021) 1445–1451. https://doi.org/10.1016/j.ijbiomac.2020.11.098.

[108] P. Ahlin Grabnar, J. Kristl, Physicochemical characterization of protein-loaded pectin-chitosan nanoparticles prepared by polyelectrolyte complexation, Pharmazie. 65 (2010) 851–852. https://doi.org/10.1691/ph.2010.0197.

[109] M.R. Avadi, A.M.M. Sadeghi, N. Mohammadpour, S. Abedin, F. Atyabi, R. Dinarvand, M.

Rafiee-Tehrani, Preparation and characterization of insulin nanoparticles using chitosan and Arabic gum with ionic gelation method, Nanomedicine Nanotechnology, Biol. Med. 6 (2010) 58–63. https://doi.org/10.1016/j.nano.2009.04.007.

[110] L. Fan, H. Wu, H. Zhang, F. Li, T. Yang, C. Gu, Q. Yang, Novel super pH-sensitive nanoparticles responsive to tumor extracellular pH, Carbohydr. Polym. 73 (2008) 390–400. https://doi.org/10.1016/j.carbpol.2007.12.006.

[111] T. Kiang, C. Bright, C.Y. Cheung, P.S. Stayton, A.S. Hoffman, K.W. Leong, Formulation of chitosan-DNA nanoparticles with poly(propyl acrylic acid) enhances gene expression, J. Biomater. Sci. Polym. Ed. 15 (2004) 1405–1421. https://doi.org/10.1163/1568562042368112.

[112] J.. Chung, M. Yokoyama, M. Yamato, T. Aoyagi, Y. Sakurai, T. Okano, Thermo-responsive drug delivery from polymeric micelles constructed using block copolymers of poly(N-isopropylacrylamide) and poly(butylmethacrylate), J. Control. Release. 62 (1999) 115–127. https://doi.org/10.1016/S0168-3659(99)00029-2.

[113] N.S. Rejinold, K.P. Chennazhi, S.V. Nair, H. Tamura, R. Jayakumar, Biodegradable and thermo-sensitive chitosan-g-poly(N-vinylcaprolactam) nanoparticles as a 5-fluorouracil carrier, Carbohydr. Polym. 83 (2011) 776–786. https://doi.org/10.1016/j.carbpol.2010.08.052.

[114] S. Mansouri, Y. Cuie, F. Winnik, Q. Shi, P. Lavigne, M. Benderdour, E. Beaumont, J.C. Fernandes, Characterization of folate-chitosan-DNA nanoparticles for gene therapy, Biomaterials. 27 (2006) 2060–2065. https://doi.org/10.1016/j.biomaterials.2005.09.020.

[115] M. Chandrasekaran, K.D. Kim, S.C. Chun, Antibacterial activity of chitosan nanoparticles: A review, Processes. 8 (2020) 1–21. https://doi.org/10.3390/PR8091173.

[116] A. Grenha, Chitosan nanoparticles: A survey of preparation methods, J. Drug Target. 20 (2012) 291–300. https://doi.org/10.3109/1061186X.2011.654121.

[117] K. Divya, M.S. Jisha, Chitosan nanoparticles preparation and applications, Environ. Chem. Lett. 16 (2018) 101–112. https://doi.org/10.1007/s10311-017-0670-y.

[118] A. Klibanov, Targeted delivery of gas-filled microspheres, contrast agents for ultrasound imaging, Adv. Drug Deliv. Rev. 37 (1999) 139–157. https://doi.org/10.1016/S0169-409X(98)00104-5.

[119] M.J. Borrelli, W.D. O'Brien, L.J. Bernock, H.R. Williams, E. Hamilton, J. Wu, M.L. Oelze, W.C. Culp, Production of uniformly sized serum albumin and dextrose microbubbles, Ultrason. Sonochem. 19 (2012) 198–208. https://doi.org/10.1016/j.ultsonch.2011.05.010.

[120] J. Owen, C. Crake, J.Y. Lee, D. Carugo, E. Beguin, A.A. Khrapitchev, R.J. Browning, N. Sibson, E. Stride, A versatile method for the preparation of particle-loaded microbubbles for multimodality imaging and targeted drug delivery, Drug Deliv. Transl. Res. 8 (2018) 342–356. https://doi.org/10.1007/s13346-017-0366-7.

[121] Y. Gao, C.U. Chan, Q. Gu, X. Lin, W. Zhang, D.C.L. Yeo, A.M. Alsema, M. Arora, M.S.K. Chong, P. Shi, C.-D. Ohl, C. Xu, Controlled nanoparticle release from stable magnetic microbubble oscillations, NPG Asia Mater. 8 (2016) e260–e260. https://doi.org/10.1038/am.2016.37.

[122] E. Unger, T. McCreer, D. Yellowhair, T.R. Barrette, Apparatus and method for making gas-

filled vesicles of optimal size, 1997. https://patents.google.com/patent/US5656211A/en.

[123] A. V. Postnikov, I. V. Uvarov, N. V. Penkov, V.B. Svetovoy, Collective behavior of bulk nanobubbles produced by alternating polarity electrolysis, Nanoscale. 10 (2018) 428–435. https://doi.org/10.1039/C7NR07126D.

[124] R. Chen, P.-F. Dong, J.-H. Xu, Y.-D. Wang, G.-S. Luo, Controllable microfluidic production of gas-in-oil-in-water emulsions for hollow microspheres with thin polymer shells, Lab Chip. 12 (2012) 3858. https://doi.org/10.1039/c2lc40387k.

[125] E. Castro-Hernández, W. van Hoeve, D. Lohse, J.M. Gordillo, Microbubble generation in a co-flow device operated in a new regime, Lab Chip. 11 (2011) 2023. https://doi.org/10.1039/c0lc00731e.

[126] M. Schneider, SonoVue, a new ultrasound contrast agent, Eur. Radiol. 9 (1999) S347–S348. https://doi.org/10.1007/PL00014071.

[127] S. Podell, C. Burrascano, M. Gaal, B. Golec, J. Maniquis, P. Mehlhaff, Physical and biochemical stability of Optison®, an injectable ultrasound contrast agent, Biotechnol. Appl. Biochem. 30 (1999) 213–223. https://doi.org/10.1111/j.1470-8744.1999.tb00773.x.

[128] F. Cavalieri, M. Ashokkumar, F. Grieser, F. Caruso, Ultrasonic Synthesis of Stable, Functional Lysozyme Microbubbles, Langmuir. 24 (2008) 10078–10083. https://doi.org/10.1021/la801093q.

[129] E.Y. Lukianova-Hleb, X. Ren, J.A. Zasadzinski, X. Wu, D.O. Lapotko, Plasmonic Nanobubbles Enhance Efficacy and Selectivity of Chemotherapy Against Drug-Resistant Cancer Cells, Adv. Mater. 24 (2012) 3831–3837. https://doi.org/10.1002/adma.201103550.

[130] W. Liu, S. Wen, L. Jiang, X. An, M. Zhang, H. Wang, Z. Zhang, G. Zhang, X. Shi, PLGA Hollow Microbubbles Loaded with Iron Oxide Nanoparticles and Doxorubicin for Dual-mode US/MR Imaging and Drug Delivery, Curr. Nanosci. 10 (2014) 543–552. https://doi.org/10.2174/15734137106661404292239 27.

[131] R. Gramiak, P.M. Shah, D.H. Kramer, Ultrasound Cardiography: Contrast Studies in Anatomy and Function, Radiology. 92 (1969) 939–948. https://doi.org/10.1148/92.5.939.

[132] F.S. Villanueva, W.R. Wagner, Ultrasound molecular imaging of cardiovascular disease, Nat. Clin. Pract. Cardiovasc. Med. 5 (2008) S26–S32. https://doi.org/10.1038/ncpcardio1246.

[133] I. Lentacker, S.C. De Smedt, N.N. Sanders, Drug loaded microbubble design for ultrasound triggered delivery, Soft Matter. 5 (2009) 2161. https://doi.org/10.1039/b823051j.

[134] K.W. Ferrara, M.A. Borden, H. Zhang, Lipid-Shelled Vehicles: Engineering for Ultrasound Molecular Imaging and Drug Delivery, Acc. Chem. Res. 42 (2009) 881–892. https://doi.org/10.1021/ar8002442.

[135] H. Leong-Poi, M.A. Kuliszewski, M. Lekas, M. Sibbald, K. Teichert-Kuliszewska, A.L. Klibanov, D.J. Stewart, J.R. Lindner, Therapeutic Arteriogenesis by Ultrasound-Mediated VEGF 165 Plasmid Gene Delivery to Chronically Ischemic Skeletal Muscle, Circ. Res. 101 (2007) 295–303. https://doi.org/10.1161/CIRCRESAHA.107.148676.

[136] H. Dewitte, S. Van Lint, C. Heirman, K. Thielemans, S.C. De Smedt, K. Breckpot, I. Lentacker, The potential of antigen and TriMix sonoporation using mRNA-loaded microbubbles for ultrasound-triggered cancer immunotherapy, J. Control. Release. 194

(2014) 28–36. https://doi.org/10.1016/j.jconrel.2014.08.011.

[137] L. Zhang, Y. Zhang, X. Zhang, Z. Li, G. Shen, M. Ye, C. Fan, H. Fang, J. Hu, Electrochemically Controlled Formation and Growth of Hydrogen Nanobubbles, Langmuir. 22 (2006) 8109–8113. https://doi.org/10.1021/la060859f.

[138] P. Bhandari, X. Wang, J. Irudayaraj, Oxygen Nanobubble Tracking by Light Scattering in Single Cells and Tissues, ACS Nano. 11 (2017) 2682–2688. https://doi.org/10.1021/acsnano.6b07478.

[139] E.C. Unger, T. Porter, W. Culp, R. Labell, T. Matsunaga, R. Zutshi, Therapeutic applications of lipid-coated microbubbles, Adv. Drug Deliv. Rev. 56 (2004) 1291–1314. https://doi.org/10.1016/j.addr.2003.12.006.

[140] P.M. Winter, K. Cai, S.D. Caruthers, S.A. Wickline, G.M. Lanza, Emerging nanomedicine opportunities with perfluorocarbon nanoparticles, Expert Rev. Med. Devices. 4 (2007) 137–145. https://doi.org/10.1586/17434440.4.2.137.

[141] R. Cavalli, A. Bisazza, M. Trotta, M. Argenziano, A. Civra, M. Donalisio, D. Lembo, New chitosan nanobubbles for ultrasound-mediated gene delivery: Preparation and in vitro characterization, Int. J. Nanomedicine. 7 (2012) 3309–3318. https://doi.org/10.2147/IJN.S30912.

[142] R. Pasupathy, P. Pandian, S. Selvamuthukumar, Nanobubbles: A Novel Targeted Drug Delivery System, Brazilian J. Pharm. Sci. 58 (2022) 1–22. https://doi.org/10.1590/s2175-97902022e19604.

[143] R. Villa, B. Cerroni, L. Viganò, S. Margheritelli, G. Abolafio, L. Oddo, G. Paradossi, N. Zaffaroni, Targeted doxorubicin delivery by chitosan-galactosylated modified polymer microbubbles to hepatocarcinoma cells, Colloids Surfaces B Biointerfaces. 110 (2013) 434–442. https://doi.org/10.1016/j.colsurfb.2013.04.022.

[144] R. Bekeredjian, S. Chen, P.A. Grayburn, R. V. Shohet, Augmentation of cardiac protein delivery using ultrasound targeted microbubble destruction, Ultrasound Med. Biol. 31 (2005) 687–691. https://doi.org/10.1016/j.ultrasmedbio.2004.08.002.

[145] C. Magnetto, M. Prato, A. Khadjavi, G. Giribaldi, I. Fenoglio, J. Jose, G.R. Gulino, F. Cavallo, E. Quaglino, E. Benintende, G. Varetto, A. Troia, R. Cavalli, C. Guiot, Ultrasound-activated decafluoropentane-cored and chitosan-shelled nanodroplets for oxygen delivery to hypoxic cutaneous tissues, RSC Adv. 4 (2014) 38433–38441. https://doi.org/10.1039/C4RA03524K.

[146] I. Lentacker, I. De Cock, R. Deckers, S.C. De Smedt, C.T.W. Moonen, Understanding ultrasound induced sonoporation: Definitions and underlying mechanisms, Adv. Drug Deliv. Rev. 72 (2014) 49–64. https://doi.org/10.1016/j.addr.2013.11.008.

[147] F.D. Moghaddam, E.N. Zare, M. Hassanpour, F.R. Bertani, A. Serajian, S.F. Ziaei, A.C. Paiva-Santos, R.E. Neisiany, P. Makvandi, S. Iravani, Y. Xu, Chitosan-based nanosystems for cancer diagnosis and therapy: Stimuli-responsive, immune response, and clinical studies, Carbohydr. Polym. 330 (2024) 121839. https://doi.org/10.1016/j.carbpol.2024.121839.

[148] D. Chen, H. Yu, H. Mu, J. Wei, Z. Song, H. Shi, R. Liang, K. Sun, W. Liu, Novel chitosan derivative for temperature and ultrasound dual-sensitive liposomal microbubble gel, Carbohydr. Polym. 94 (2013) 17–23. https://doi.org/10.1016/j.carbpol.2012.12.069.

[149] X. Rong, Y. Ji, X. Zhu, J. Yang, D. Qian, X. Mo, Y. Lu, Neuroprotective effect of insulin-loaded chitosan nanoparticles/PLGA-PEG-PLGA hydrogel on diabetic retinopathy in rats, Int. J. Nanomedicine. Volume 14 (2018) 45–55. https://doi.org/10.2147/IJN.S184574.

[150] M.S. Riederer, B.D. Requist, K.A. Payne, J.D. Way, M.D. Krebs, Injectable and microporous scaffold of densely-packed, growth factor-encapsulating chitosan microgels, Carbohydr. Polym. 152 (2016) 792–801. https://doi.org/10.1016/j.carbpol.2016.07.052.

[151] Y.-Y. Fu, L. Zhang, Y. Yang, C. Liu, Y.-N. He, P. Li, X. Yu, Synergistic antibacterial effect of ultrasound microbubbles combined with chitosan-modified polymyxin B-loaded liposomes on biofilm-producing Acinetobacter baumannii, Int. J. Nanomedicine. Volume 14 (2019) 1805–1815. https://doi.org/10.2147/IJN.S186571.

[152] W.J.M. Mulder, G.J. Strijkers, G.A.F. van Tilborg, A.W. Griffioen, K. Nicolay, Lipid-based nanoparticles for contrast-enhanced MRI and molecular imaging, NMR Biomed. 19 (2006) 142–164. https://doi.org/10.1002/nbm.1011.

[153] S.K. Das, N. Putra, W. Roetzel, Pool boiling characteristics of nano-fluids, Int. J. Heat Mass Transf. 46 (2003) 851–862. https://doi.org/10.1016/S0017-9310(02)00348-4.

[154] M. Arora, C.D. Ohl, K.A. Mørch, Cavitation inception on microparticles: A self-propelled particle accelerator, Phys. Rev. Lett. 92 (2004) 1–4. https://doi.org/10.1103/PhysRevLett.92.174501.

[155] K. Yasui, T. Tuziuti, W. Kanematsu, K. Kato, Dynamic Equilibrium Model for a Bulk Nanobubble and a Microbubble Partly Covered with Hydrophobic Material, Langmuir. 32 (2016) 11101–11110. https://doi.org/10.1021/acs.langmuir.5b04703.

[156] V. HOVEN, V. TANGPASUTHADOL, Y. ANGKITPAIBOON, N. VALLAPA, S. KIATKAMJORNWONG, Surface-charged chitosan: Preparation and protein adsorption, Carbohydr. Polym. 68 (2007) 44–53. https://doi.org/10.1016/j.carbpol.2006.07.008.

[157] C.E. Brennen, Phase Change, Nucleation, and Cavitation, 2013. https://doi.org/10.1017/cbo9781107338760.002.

[158] Y.L. Liu, Y.H. Wu, W.B. Tsai, C.C. Tsai, W.S. Chen, C.S. Wu, Core-shell silica@chitosan nanoparticles and hollow chitosan nanospheres using silica nanoparticles as templates: Preparation and ultrasound bubble application, Carbohydr. Polym. 84 (2011) 770–774. https://doi.org/10.1016/j.carbpol.2010.03.033.

[159] A. Ebrahiminia, M. Mokhtari-Dizaji, T. Toliyat, Correlation between iodide dosimetry and terephthalic acid dosimetry to evaluate the reactive radical production due to the acoustic cavitation activity, Ultrason. Sonochem. 20 (2013) 366–372. https://doi.org/10.1016/j.ultsonch.2012.05.016.

[160] M.A. Nugent, R. V Iozzo, Fibroblast growth factor-2, Int. J. Biochem. Cell Biol. 32 (2000) 115–120. https://doi.org/10.1016/S1357-2725(99)00123-5.

[161] K. Obara, M. Ishihara, T. Ishizuka, M. Fujita, Y. Ozeki, T. Maehara, Y. Saito, H. Yura, T. Matsui, H. Hattori, M. Kikuchi, A. Kurita, Photocrosslinkable chitosan hydrogel containing fibroblast growth factor-2 stimulates wound healing in healing-impaired db/db mice, Biomaterials. 24 (2003) 3437–3444. https://doi.org/10.1016/S0142-9612(03)00220-5.

[162] F. Andrade, F. Antunes, A. Vanessa Nascimento, S. Baptista da Silva, J. das Neves, D. Ferreira, B. Sarmento, Chitosan Formulations as Carriers for Therapeutic Proteins, Curr.

Drug Discov. Technol. 8 (2011) 157–172. https://doi.org/10.2174/157016311796799035.

[163] C.T. Nguyen, T.T. Nguyen, T.T. Nguyen, P.P.T. Nguyen, A.D. Nguyen, L.T. Tran, H. Tran-Van, Preparation and in vitro evaluation of FGF-2 incorporated carboxymethyl chitosan nanoparticles, Carbohydr. Polym. 173 (2017) 114–120. https://doi.org/10.1016/j.carbpol.2017.05.080.

[164] Y. Tao, I.B. Black, E. DiCicco-Bloom, Neurogenesis in neonatal rat brain is regulated by peripheral injection of basic fibroblast growth factor (bFGF), J. Comp. Neurol. 376 (1996) 653–663. https://doi.org/10.1002/(SICI)1096-9861(19961223)376:4<653::AID-CNE11>3.0.CO;2-N.

[165] S. Vemuri, I. Beylin, V. Sluzky, P. Stratton, G. Eberlein, Y.J. Wang, The Stability of bFGF Against Thermal Denaturation, J. Pharm. Pharmacol. 46 (2011) 481–486. https://doi.org/10.1111/j.2042-7158.1994.tb03831.x.

[166] S.J. Paluck, T.H. Nguyen, J.P. Lee, H.D. Maynard, A Heparin-Mimicking Block Copolymer Both Stabilizes and Increases the Activity of Fibroblast Growth Factor 2 (FGF2), Biomacromolecules. 17 (2016) 3386–3395. https://doi.org/10.1021/acs.biomac.6b01182.

[167] Z. Ali, A. Islam, P. Sherrell, M. Le-Moine, G. Lolas, K. Syrigos, M. Rafat, L.D. Jensen, Adjustable delivery of pro-angiogenic FGF-2 by collagen-alginate microspheres, Biol. Open. (2018). https://doi.org/10.1242/bio.027060.

[168] H.A.E. Benson, A.C. Watkinson, Transdermal and topical drug delivery: principles and practice, John Wiley & Sons, Inc., 2012. https://doi.org/10.1007/3-540-26869-3_2.

[169] X. Xie, Y. Kurashina, M. Matsui, T. Nomoto, M. Itoh, H.J. Okano, K. Nakamura, N. Nishiyama, Y. Kitamoto, Transdermal delivery of bFGF with sonophoresis facilitated by chitosan nanocarriers, J. Drug Deliv. Sci. Technol. 75 (2022) 103675. https://doi.org/10.1016/j.jddst.2022.103675.

[170] Y. Xu, Y. Du, Effect of molecular structure of chitosan on protein delivery properties of chitosan nanoparticles, Int. J. Pharm. 250 (2003) 215–226. https://doi.org/10.1016/S0378-5173(02)00548-3.

[171] E.J. Chang, J.K. Kundu, L. Liu, J.W. Shin, Y.J. Surh, Ultraviolet B radiation activates NF-κB and induces iNOS expression in HR-1 hairless mouse skin: Role of IκB kinase-β, Mol. Carcinog. 50 (2011) 310–317. https://doi.org/10.1002/mc.20646.

[172] B.E. Polat, D. Blankschtein, R. Langer, Low-frequency sonophoresis: Application to the transdermal delivery of macromolecules and hydrophilic drugs, Expert Opin. Drug Deliv. 7 (2010) 1415–1432. https://doi.org/10.1517/17425247.2010.538679.

[173] N. Dragicevic, H.I. Maibach, Percutaneous penetration enhancers physical methods in penetration enhancement, 2017. https://doi.org/10.1007/978-3-662-53273-7.

[174] M.A. Oberli, C.M. Schoellhammer, R. Langer, D. Blankschtein, Ultrasound-enhanced transdermal delivery: recent advances and future challenges, Ther. Deliv. 5 (2014) 843–857. https://doi.org/10.4155/tde.14.32.

[175] F. Larese Filon, M. Mauro, G. Adami, M. Bovenzi, M. Crosera, Nanoparticles skin absorption: New aspects for a safety profile evaluation, Regul. Toxicol. Pharmacol. 72 (2015) 310–322. https://doi.org/10.1016/j.yrtph.2015.05.005.

[176] S. Merouani, O. Hamdaoui, F. Saoudi, M. Chiha, Influence of experimental parameters on

sonochemistry dosimetries: KI oxidation, Fricke reaction and H2O2 production, J. Hazard. Mater. 178 (2010) 1007–1014. https://doi.org/10.1016/j.jhazmat.2010.02.039.

[177] Y. Iida, K. Yasui, T. Tuziuti, M. Sivakumar, Sonochemistry and its dosimetry, Microchem. J. 80 (2005) 159–164. https://doi.org/10.1016/j.microc.2004.07.016.

[178] S. Koda, T. Kimura, T. Kondo, H. Mitome, A standard method to calibrate sonochemical efficiency of an individual reaction system, Ultrason. Sonochem. 10 (2003) 149–156. https://doi.org/10.1016/S1350-4177(03)00084-1.

[179] B. Kratochvíl, V. Mornstein, Use of Chemical Dosimetry for Comparison of Ultrasound and Ionizing Radiation Effects on Cavitation, Physiol. Res. 56 (2007) S77–S84. https://doi.org/10.33549/physiolres.931378.

[180] T.J.J. Mason, J.P.P. Lorimer, D.M.M. Bates, Y. Zhao, Dosimetry in sonochemistry: the use of aqueous terephthalate ion as a fluorescence monitor, Ultrason. Sonochem. 1 (1994) S91–S95. https://doi.org/10.1016/1350-4177(94)90004-3.

[181] A.H. Barati, M. Mokhtari-Dizaji, H. Mozdarani, Z. Bathaie, Z.M. Hassan, Effect of exposure parameters on cavitation induced by low-level dual-frequency ultrasound, Ultrason. Sonochem. 14 (2007) 783–789. https://doi.org/10.1016/j.ultsonch.2006.12.016.

Acknowledgements

I would like to express my sincere gratitude to all those who have supported me throughout my doctoral journey. First and foremost, I would like to thank my advisor, Professor Yoshitaka Kitamoto, for the invaluable guidance, encouragement, and patience. The insights and expertise have been instrumental in shaping this dissertation.

I am also grateful to Assistant Professor Kyohei Okubo for his warm encouragement and valuable suggestions during every seminar. I also would like to thank Yuta Kurashina, who has no longer worked here. His guidance and assistance were invaluable, and I wish him all the best in his new position.

I would like to express my appreciation to my thesis panels: Professor Masato Sone, Professor Kentaro Nakamura, Associate Professor Tomohiro Hayashi and Associate Professor Hiroyuki Wada for their constructive comments, sincere suggestions, and honest assessments that helped to improve this dissertation.

I owe a special thanks to my family for their unwavering love and encouragement. I would also like to acknowledge my friends and all the laboratory members who have been a part of this journey. Additionally, I want to extend my gratitude to very special little friends, Tutu, Xiaolv, Atie, Ningmeng and Xiaohu. Your presence has brought joy and light into my life, and your playful spirits have been a delightful source of inspiration during this challenging process.

Finally, I would like to thank all those who have contributed to this dissertation in any way. Your support has been greatly appreciated.

Accomplishment

Journal Publication

1. X. Xie, Y. Kurashina, M. Matsui, T. Nomoto, M. Itoh, H.J. Okano, K. Nakamura, N. Nishiyama, Y. Kitamoto, Transdermal delivery of bFGF with sonophoresis facilitated by chitosan nanocarriers, J. Drug Deliv. Sci. Technol. 75 (2022) 103675. https://doi.org/10.1016/j.jddst.2022.103675.
2. X. Xie, Y. Kurashina, K. Okubo, H. Wada, Y. Kitamoto, Enhancement of acoustic cavitation using chitosan nanoparticle-shelled composites, Jpn. J. Appl. Phys (Accepted).